The study of graphene impact on the biocompatibility of a porous polycaprolactone surface

Lukáš Pilčík

Bachelor's thesis
2023

Tomas Bata University in Zlín
Faculty of Technology

ZADÁNÍ BAKALÁŘSKÉ PRÁCE

(projektu, uměleckého díla, uměleckého výkonu)

Jméno a příjmení:	**Lukáš Pilčík**
Osobní číslo:	**T20433**
Studijní program:	**B0711A130009 Materiály a technologie**
Specializace:	**Materiálové inženýrství**
Forma studia:	**Prezenční**
Téma práce:	**Studium vlivu grafenu na biokompatibilitu povrchu porézního polykaprolaktonu**

Zásady pro vypracování

Vedle vynikajících elektronických (vysoká pohyblivost nosičů náboje), optických (transmisivita 97,3 %) a mechanických (pevnost 1 TPa) vlastností se grafen vyznačuje vysokou biokompatibilitou, nezvyklou pro jiné elektronické materiály. Cílem této bakalářské práce je otestovat možnosti zvýšení biokompatibility povrchu porézního polykaprolaktonu pomocí grafenu. Grafen připravený chemickou depozicí z plynné fáze (CVD) bude nanášen na vhodné povrchy polykaprolaktonu mokrým přenosem (wet-transfer), jeho přítomnost bude ověřována pomocí Ramanovy spektroskopie a závěrečný test biokompatibility bude proveden měřením cytotoxicity a proliferace fibroblastů na čistém povrchu PCL a povrchu ošetřeném grafenovou vrstvou.

Dílčí cíle:

1. Proveďte rešerši uvedené problematiky.
2. Připravte vhodné povrchy PCL.
3. Naneste grafen a ověřte jeho přítomnost pomocí Ramanovy spektroskopie.
4. Porovnejte cytotoxicitu a proliferaci fibroblastů na čistém a grafenem pokrytém PCL.

Forma zpracování bakalářské práce: **tištěná/elektronická**
Jazyk zpracování: **Angličtina**

Seznam doporučené literatury:

GEIM, A. K., NOVOSELOV, K. S. The Rise of Graphene. *Nature Materials* [online]. 2007, vol. 6, no. 6, s. 183-191. ISSN 1476--1122. Dostupné z: https://www.nature.com/articles/nmat1849.
NOVOSELOV, K. S. et al. A roadmap for graphene. *Nature* [online]. 2012, vol. 490, no. 7419, s. 192-200. ISSN 0028-0836. Dostupné z: https://www.ncbi.nlm.nih.gov/pubmed/23060189.
WRZECIONKO, Erik et al. Variations of polymer porous surface structures via the time-sequenced dosing of mixed solvents. *American Chemical Society* [online]. 2017, 6472 s. ISBN 1944-82440. Dostupné z: http://dx.doi.org/10.1021/acsami.6b15774.

Vedoucí bakalářské práce: **doc. Ing. Miroslav Bartošík, Ph.D.**
Ústav fyziky a mater. inženýrství

Datum zadání bakalářské práce: **31. prosince 2022**
Termín odevzdání bakalářské práce: **19. května 2023**

L.S.

prof. Ing. Roman Čermák, Ph.D.
děkan

doc. Mgr. Aleš Mráček, Ph.D.
ředitel ústavu

Ve Zlíně dne 20. února 2023

PROHLÁŠENÍ AUTORA
BAKALÁŘSKÉ PRÁCE

Beru na vědomí, že:

- bakalářská práce bude uložena v elektronické podobě v univerzitním informačním systému a dostupná k nahlédnutí;
- na moji bakalářskou práci se plně vztahuje zákon č. 121/2000 Sb. o právu autorském, o právech souvisejících s právem autorským a o změně některých zákonů (autorský zákon) ve znění pozdějších právních předpisů, zejm. § 35 odst. 3;
- podle § 60 odst. 1 autorského zákona má Univerzita Tomáše Bati ve Zlíně právo na uzavření licenční smlouvy o užití školního díla v rozsahu § 12 odst. 4 autorského zákona;
- podle § 60 odst. 2 a 3 autorského zákona mohu užít své dílo – bakalářskou práci nebo poskytnout licenci k jejímu využití jen s předchozím písemným souhlasem Univerzity Tomáše Bati ve Zlíně, která je oprávněna v takovém případě ode mne požadovat přiměřený příspěvek na úhradu nákladů, které byly Univerzitou Tomáše Bati ve Zlíně na vytvoření díla vynaloženy (až do jejich skutečné výše);
- pokud bylo k vypracování bakalářské práce využito softwaru poskytnutého Univerzitou Tomáše Bati ve Zlíně nebo jinými subjekty pouze ke studijním a výzkumným účelům (tj. k nekomerčnímu využití), nelze výsledky bakalářské práce využít ke komerčním účelům;
- pokud je výstupem bakalářské práce jakýkoliv softwarový produkt, považují se za součást práce rovněž i zdrojové kódy, popř. soubory, ze kterých se projekt skládá. Neodevzdání této součásti může být důvodem k neobhájení práce.

Prohlašuji,

- že jsem na bakalářské práci pracoval samostatně a použitou literaturu jsem citoval. V případě publikace výsledků budu uveden jako spoluautor.
- že odevzdaná verze bakalářské práce a verze elektronická nahraná do IS/STAG jsou obsahově totožné.

Ve Zlíně, dne:

Jméno a příjmení studenta:

…….
podpis studenta

ABSTRAKT

Tato práce se zabývá přípravou povrchů porézního polykaprolaktonu metodou fázové separace indukované časově sekvenovaným dávkováním směsi dobrého a špatného rozpouštědla a také vlivem přítomnosti grafenu na biokompatibilitu povrchu porézního polykaprolaktonu. Dále byl studován vliv relativní vlhkosti (RH) na podobu porézní struktury, přičemž se ukázalo, že optimální texturizace povrchu je dosaženo při RH = 50 %. Připravené vzorky porézního polykaprolaktonu byly zkoumány pomocí rastrovací elektronové mikroskopie, mikroskopie atomárních sil a rovněž měřením kontaktního úhlu. Grafenová monovrstva vyrostlá metodou CVD byla nanesena na vybrané porézní vzorky metodou mokrého přenosu. Přítomnost grafenu na vystouplých místech porézního povrchu byla ověřena pomocí Ramanovy spektroskopie. Výsledky testů buněčné proliferace dokázaly, že nanesená grafenová vrstva značně podporuje buněčnou proliferaci.

Klíčová slova: porézní povrch, polykaprolakton, grafen, fázová separace, proliferace

ABSTRACT

This thesis deals with the preparation of porous polycaprolactone surfaces using the method of phase separation induced by time-sequenced dosing of a mixture of good and poor solvent and the effect of graphene's presence on the biocompatibility of porous polycaprolactone structure. Furthermore, the impact of relative humidity (RH) on the resulting structure was studied, whereas it has been shown that an optimal surface texturization is achieved for RH = 50 %. The prepared porous structures were examined using scanning electron microscopy, atomic force microscopy and contact angle measurement. A CVD-grown graphene monolayer was deposited on a chosen porous structure using the wet transfer method. The presence of graphene on a porous polycaprolactone surface was confirmed by Raman spectroscopy. The cell proliferation test results have proved that graphene strongly supports cell proliferation on a porous polycaprolactone surface.

Keywords: porous surface, polycaprolactone, graphene, phase separation, proliferation

I would like to thank Assoc. Prof. Miroslav Bartošík, MSc., Ph.D. for his valuable guidance and time he devoted to assisting me with the work on both theoretical and experimental part of this thesis.

I would also like to thank Lenka Musilová, MSc., PhD for her assistance regarding the preparation of polymer solutions and purification of polymer samples.

Last but not least, I would like to thank Jakub Piastek, MSc. for his assistance and helpfulness with graphene transfer onto polymer samples.

My thanks also go to my family for their unwavering support during my studies.

I hereby declare that the print version of my Bachelor's thesis and the electronic version of my thesis deposited in the IS/STAG system are identical.

„If you perceive that there are four possible ways in which a procedure can go wrong, and circumvent these, then a fifth way, unprepared for, will promptly develop“

Murphy's Sixth Law

CONTENTS

INTRODUCTION

Since the invention of fully synthetic plastics in the early 20th century, polymer materials have gradually become an integral part of various industrial sectors. In the course of year, the apparent environmental impact of traditional plastics has driven the demand for more sustainable and biocompatible alternatives. This demand has resulted in the utilization of polymer materials in the field of pharmacy and medical engineering. Biomaterials have found significant applications in regenerative medicine and tissue engineering, as these materials posses specific properties that can enhance cell proliferation and facilitate the tissue regeneration process.

One of the crucial aspects of biomaterial design is the surface properties, as the first interaction between cells and the material occurs on the surface. Therefore, the recent research is focused on tailoring or adjusting the surface properties to establish optimal conditions for cell adhesion, proliferation, and differentiation.

In addition to conventional polymer surface treatment methods like plasma treatment, as well as methods that will be mentioned in this thesis such as breath figures or phase separation, the surface properties may also be adjusted if two materials showing substantial biocompatibility would be combined. In this thesis, the focus will be on the combination of polycaprolactone and graphene, both of which have demonstrated great potential in the field of tissue engineering

Theoretical part of this thesis will be focused on porous polymer materials and methods of their preparation, graphene properties and methods of synthesis and theoretical description of experimental procedures that will be used in this work.

Experimental part will investigate the preparation of various polycaprolactone porous structures, together with the effect of relative humidity on resulting structures. Furthermore, results of various characterization methods will be presented. On a suitable porous polycaprolactone structure, a CVD-grown graphene monolayer will be transferred and its effect on the biocompatibility of porous polycaprolactone surface will be evaluated on the basis of cell proliferation results.

I. THEORY

1 POROUS POLYMER MATERIALS

Porous polymer materials have attracted considerable research interest owing to their unique ability to combine the advantageous characteristics of both porous materials and polymers. This is primarily attributed to the high surface area and well-defined porosity exhibited by porous polymers, making them an attractive choice for various applications. Furthermore, the versatility of porous polymers allows for their fabrication as thin films, further expanding their potential uses in diverse fields [1].

Porous polymers can be used as a photonic band gap, gas storage, antireflection coating [1] physically unclonable function (PUF) for anti-counterfeiting applications [2] or scaffolds for tissue engineering [3].

Porous polymers exhibit several significant structural characteristics, including pore size, functionality, topology and geometry [1]. According to IUPAC and its recommendations for the characterization of porous solids [4], the pores can be classified according to their availability to an external fluid, as shown in Fig. 1:

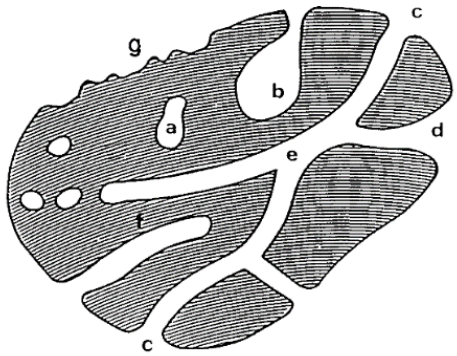

Fig. 1: Illustration of pores classification, closed pores (a), open pores (b, c, d, e ,f), dead-end pores (b, f), through pores (e), [4].

1.1 Methods of synthesis

Synthesis methods of porous polymer materials include direct templating, block copolymer self-assembly, direct synthesis, interfacial polymerization, dewetting, breath figures, phase separation induced by time-sequenced dosing of mixed solvent etc. Detailed descriptions of the last two mentioned methods can be seen on the following page [1], [2], [5].

1.1.1 Breath figures

Among the many methods of porous surface preparation, the breath figures (BF) is a well-established and widely used fabrication approach based on a well-known phenomenon of ordered water droplets formation on a cold surface which is brought in contact with moist air. Generation of porous polymer structures using the BF templating method is usually achieved by casting of a polymer solution on a substrate in humid environment. By adjusting the experimental conditions, the BF pattering allows the preparation of surfaces with various pore size distribution (from nanoporous to microporous), as well as highly ordered porous structures such as honeycomb-structured films [6], [7], [8].

The pore formation process via the BF mechanism as a templating method is outlined in Fig. 2. The initial casting of a polymer solution under humid conditions is immediately followed by endothermic evaporation of the volatile solvent (Fig. 2a). This leads to a decrease of the solvent temperature, thus initiating a nucleation process and water droplets condensation on a cold surface (b). These droplets are thermodynamically stable a do not evaporate, thus are allowed to grow bigger (by coalescence). Droplets form a close pack array due to thermocapillary effects and Bénard-Marangoni convection (c). When the array cools and sinks into solution, the free surface allows further nucleation and growth of new water droplets generation (e), (f). After all the residual solvent and water evaporate, a 3-D array (g) is left behind [7], [9].

In general, a film with monolayer of ordered pores is formed if the solvent evaporates before the process of droplet coalescence begins. However, if the solvent is still present, the polymer can stabilize the water droplets (by preventing coagulation) and droplet array can sink into the solution. The formation of multi-layered porous 3-D array structures is also supported by solvent of lower density than water, although literature also mentions exemptions to this rule [7].

The size of the generated pores is mainly affected by humidity values and air flow rate. Higher relative humidity values generally lead to larger pore sizes, whereas an increase in the flow rate (thus an increase in the evaporation rate) decreases the pore size [7].

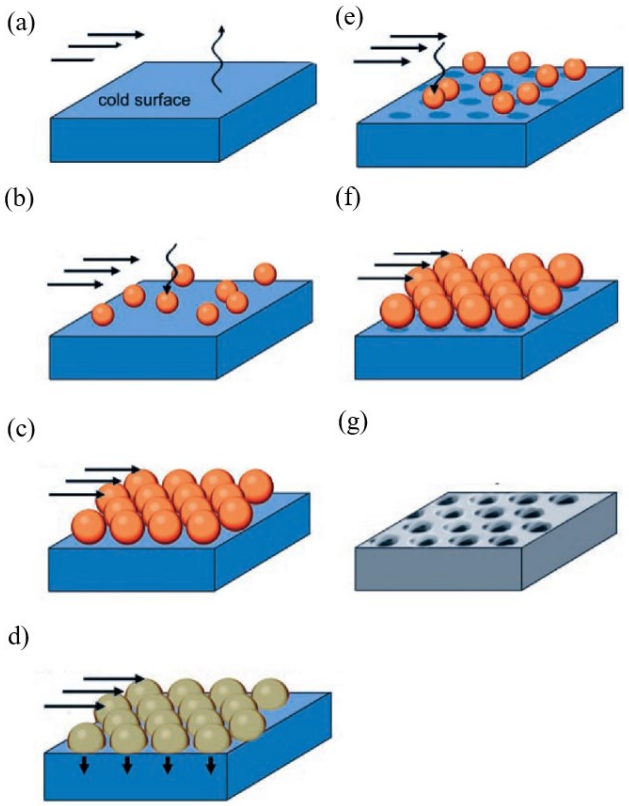

Fig. 2: Pore formation process via breath figures approach, (a) flow of moist air and solvent evaporation, (b) water condensation (nucleation), (c) water droplets form close packed array, (d) array cools and sink into solution, (e) new generation of water droplets, (f) new close packed array templated by underlying layer, (g) 3D array remains after solvent and water evaporate. Adapted from [9].

1.1.2 Phase separation induced by time sequenced dosing of mixed solvents

The preparation of porous polymer structures by the method of time sequenced dosing of mixed solvents on the rotating polymer surface associated with phase separation was described by Wrzecionko et. al. in 2017 [5]. The phase separation in this process is induced by a poor solvent. By dosing a solvent mixture onto a polymer surface, phase separation occurs as the solubility of the polymer in good and poor solvent differs. Thus, two phases are formed, one with polymer-rich solvent (good solvent) and the other with polymer-lean solvent (poor solvent). For a phase separation to occur, certain requirements must be met: good and poor solvent have to be mutually miscible and the evaporation rate of the good solvent has to be higher than that of the poor solvent [5], [10].

Individual steps of this surface modification method are schematically demonstrated on a polystyrene surface treatment in Fig. 3. In the first step (step 1), after a mixture of THF and 2-EE is dosed, THF penetrates and swells the PS surface. As the THF evaporates preferentially, the phase separation occurs resulting into formation of 2-EE microdroplets, followed by embossing of the microdroplets into the swollen layer due to the Laplace pressure. Tendency of polymer-lean phase to form spherical shape is driven by the principle of minimal surface energy. In step 2, further dosing of the solvent mixture results in an increase in the depth of the swollen layer, as well as the aggregation and growth of separated 2-EE droplets. In the final stage of this step, only 2-EE droplets in swollen PS layer are present [5].

The number and size of generated pores is determined by environment conditions and parameters such as ratio of individual components, total volume of dosed mixture, temperature of the solvent mixture and temperature gradient, rotation speed (centrifugal force), air flow rate, time sequence of individual deposition steps, evaporation rate and interfacial tension. The process of pore generation can also be significantly affected by relative humidity [5].

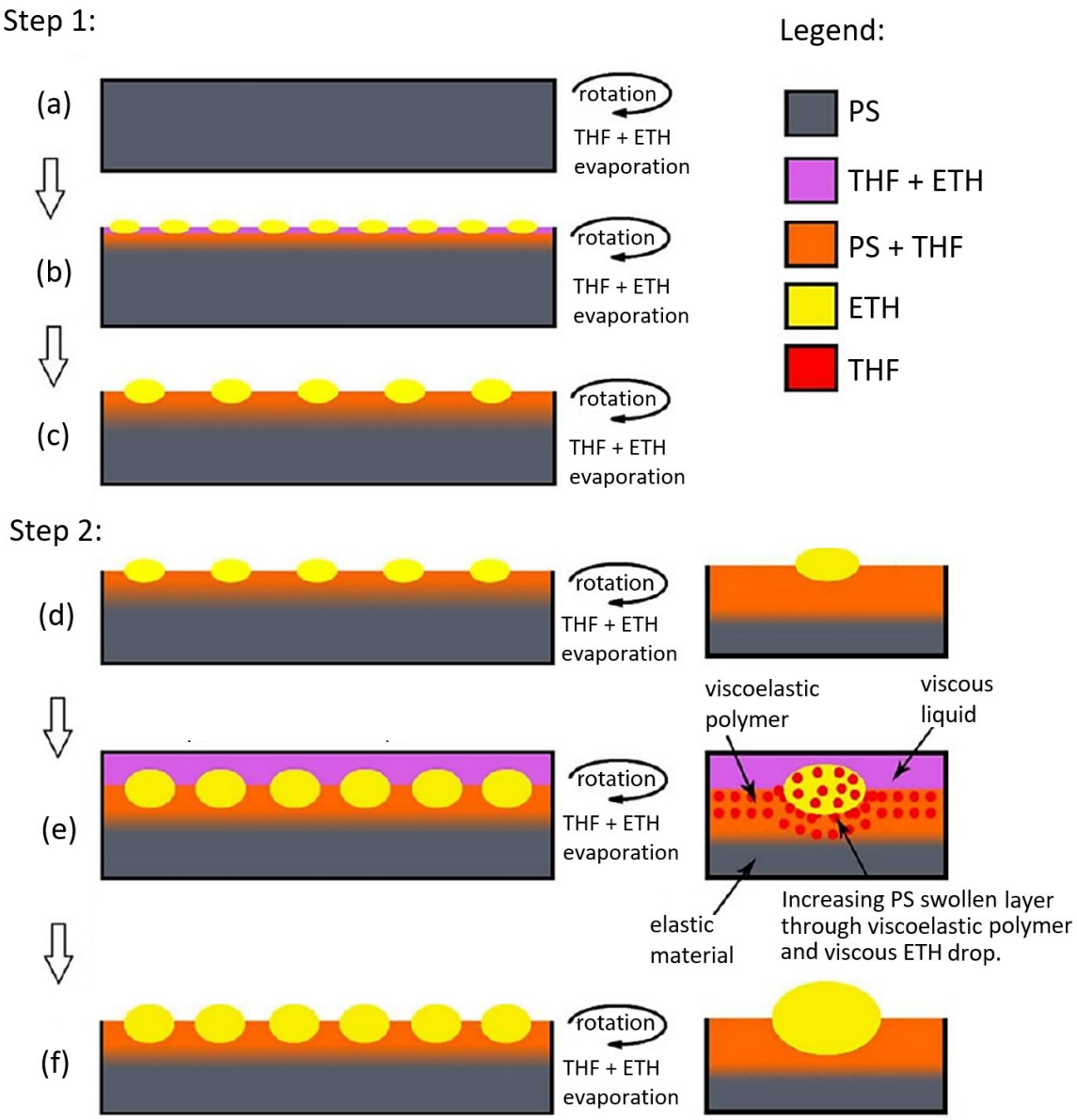

Fig. 3: Scheme of pores generation via phase separation induced by time sequenced dosing of mixed solvent, step 1: THF + ETH deposition on the surface, (b) swelling; small drop creation, dissolution; phase separation, Laplace pressure / surface tension action, (c) Laplace pressure / surface tension action; PS flow due to rapid THF evaporation, step 2: (d) second deposition / initial thickness of PS +THF and ETH diameter depends on time sequence between steps 1 and 2, (e) increasing of the PS swollen layer thickness and ETH drop diameter; aggregation of ETH in PS viscous surface; swelling; small drop creation; dissolution; phase separation; Laplace pressure / surface tension action, (f) Laplace pressure / surface tension action; PS flow due to rapid THF evaporation. Adapted from [5].

1.2 Polymer solvents

A solvent is a substance, ordinarily a liquid, which dissolves one or several substances, resulting in a solution. The process of polymer dissolution into a solvent generally consists of two steps: solvent diffusion, followed by chain disentanglement. This leads to the formation of a swollen gel layer on the interface of polymer and solvent [11].

The solubility of a polymer in solvent is determined by many factors, mainly by its chemical structure (including crystallinity), nature of the solvent and temperature of the solution [11]. Various parameters originating from thermodynamic studies are used to determine the compatibility of a given combination of polymer and solvent. The parameters commonly used in industry, thus the most important, are Flory–Huggins parameter χ (also called polymer-solvent interaction parameter) and Hildebrand solubility parameter δ [12].

1.2.1 Thermodynamic background

1.2.1.1 Flory–Huggins parameter χ

The formation of a polymer solutions, as well as the formation of solutions of low molecular weight substances, is governed by the laws of thermodynamics. The direction of the thermodynamic process, including dissolution, can be predicted from the value of the change in Gibbs free energy:

$$\Delta G_m = \Delta H_m - T\Delta S_m \tag{1}$$

where ΔG_m is the Gibbs free change energy of mixing, ΔH_m is the enthalpy change of mixing, T is the thermodynamic temperature, and ΔS_m is the entropy change of mixing. In a given low molecular weight substance (solvent), the polymer dissolves spontaneously if the value change of Gibbs free energy of mixing is negative [13].

It must be noted that Eq. (1) is valid for dissolution of an amorphous polymer. In case of the dissolution of crystalline polymers, terms containing free energy of fusion for the crystalline volume fraction would be added [13].

The miscibility of a polymer with a solvent is described by a Flory-Huggins mean-field theory. This theory uses the lattice model for polymer chains and solvent molecules arrangement. For the quantitative description of polymer solutions, volume fraction of polymer and solvent are used. Gibbs free energy of mixing can then be expressed as:

$$\frac{\Delta G}{RT} = \frac{\phi_1}{x_1} ln\, \Phi_1 + \frac{\phi_2}{x_2} ln\, \phi_2 + \chi\, \phi_1 \phi_2 \tag{2}$$

where ϕ is the volume fraction, x is the chain length with each repeating unit defined as occupying a lattice site, and R is the molar gas constant [14].

Polymer solution is a two-component system. The Flory–Huggins mean-field theory considers short-range interactions, typically hydrogen bonding and van der Waals interactions. Interactions between components of solution are described by interaction energy parameter ω. In addition to the interaction between individual polymer chains ω_{22} and interaction between molecules of solvent ω_{11}, interactions between polymer chain and solvent ω_{12} occur after mixing. The mixing of the polymer and solvent results in interaction energy changes [15]. The value of interaction energy change $\Delta\omega_{12}$ for each newly created polymer-solvent contact is equal to:

$$\Delta\omega_{12} = \omega_{12} - \frac{1}{2}(\omega_{22} + \omega_{11}) \tag{3}$$

The Flory–Huggins parameter χ parameter is defined as:

$$\chi = \frac{Z\Delta\omega_{12}}{k_B T} \tag{4}$$

where Z is the lattice coordinate, k_B is the Boltzman constant, and T is the thermodynamic temperature [15].

1.2.1.2 Hildebrand solubility parameter

For a specific compound, the Hildebrand solubility parameter δ is defined as the square root of the cohesive energy density. The cohesive energy density ΔE is the energy of vaporization per volume unit V [13].

$$\delta = \sqrt{\frac{\Delta E}{V}} \tag{5}$$

The solubility of a polymer increases as the difference of the solubility parameter of polymer δ_p and solubility parameter of solvent δ_s is getting close to zero [12].

1.2.2 Types of polymer solvents

1.2.2.1 Good solvent

A solvent with $\chi < \frac{1}{2}$ is called a good solvent. [15] As the interactions between polymer chains and solvent molecules are preferred, the presence of a good solvent causes the polymer chain to disentangle and fully expand. As a result, the surface area that can be occupied by solvent molecules increases. This leads to formation of a swollen layer. Viscosity values of such solutions are usually high [11], [16].

1.2.2.2 Poor solvent

A solvent with $\chi > 1/2$ is called a poor solvent. [15] The polymer-polymer and solvent-solvent interactions are favourable, causing the polymer chains to contract. Viscosity values of such solutions are usually low [16].

1.2.2.3 Theta solvent

Theta solvent is a solvent in which the polymer chains are present in a random coil conformation, which is due to the ideal behaviour of polymer chains. This behaviour occurs under a theta temperature when a theta condition is achieved. The theta temperature value is unique for each polymer-solvent system [15]. Under theta condition, the Gibbs free energy of mixing from Eq. (1) is equal to zero [13].

1.3 Biocompatibility assessment

Biocompatibility refers to the ability of a material to carry out its intended function without inducing any unfavourable reactions or detrimental effect upon interaction with biological system. It involves assessing the compatibility of the material with living tissues, cells, and the overall biological environment. In the field of polymer materials, assessing cell viability and cell proliferation is crucial for understanding their biocompatibility and potential applications in various biomedical fields. One commonly used method for evaluating cell viability is the MTT assay (assay for cellular metabolic activity) [17].

MTT assay is colorimetric assay utilizing the ability of viable cells to convert a yellow, water-soluble methyl-thiazolyl-tetrazolium salt (MTT) into purple, water-insoluble compound called formazan. MTT reagent is reduced to formazan by metabolically active cells, upon entering of MTT reagent through the cell and mitochondrial membranes.

Formazan crystals are extracted with suitable solvent, such as dimethyl sulfoxide (DMSO). The amount of formazan, which is directly proportional to the number of viable cells present in the sample, is estimated by spectrophotometry. Relative viability or cytotoxicity can be determined by comparing the absorbance values of experimental samples to control samples. Two main approaches commonly used in MTT assays are the direct contact method and the extract exposure method. [18], [19].

After the cytotoxicity evaluation, additional cell culture assays can be conducted to determine which of the studied samples enhance cell proliferation.

1.4 Polycaprolactone

Polycaprolactone (PCL) is a semicrystalline aliphatic polyester, generally synthesized by ring-opening polymerization of ε-caprolactone. PCL is a biocompatible, biodegradable, and nontoxic polymer with a low glass transition temperature (−60 °C) and melting temperature (60 °C). Due to its slow degradation rate, PCL is commonly used for long-term implants, drug delivery systems, and as a material for tissue engineering applications [20].

2 GRAPHENE

2.1 General characterization

Graphene is a two-dimensional planar sheet consisting of sp^2 hybridized carbon atoms tightly packed into a hexagonal lattice. Being a 2D atomic crystal, it was presumed not to exist until its discovery in 2004 by Andre Geim and Konstantin Novoselov, despite being used as a theoretical model from the late 1950s. The main argument for its non-existence was that thermal fluctuations of two-dimensional crystal lattices can cause out-of plane vibrations causing strong longitudinal tension, thus resulting in a breakdown of the lattice. However, graphene's discovery showed that even 2D crystals can be intrinsically stable by relieving the stress caused by thermal fluctuations through gentle wrapping, i. e. crumpling into the 3D dimension [21], [22], [23].

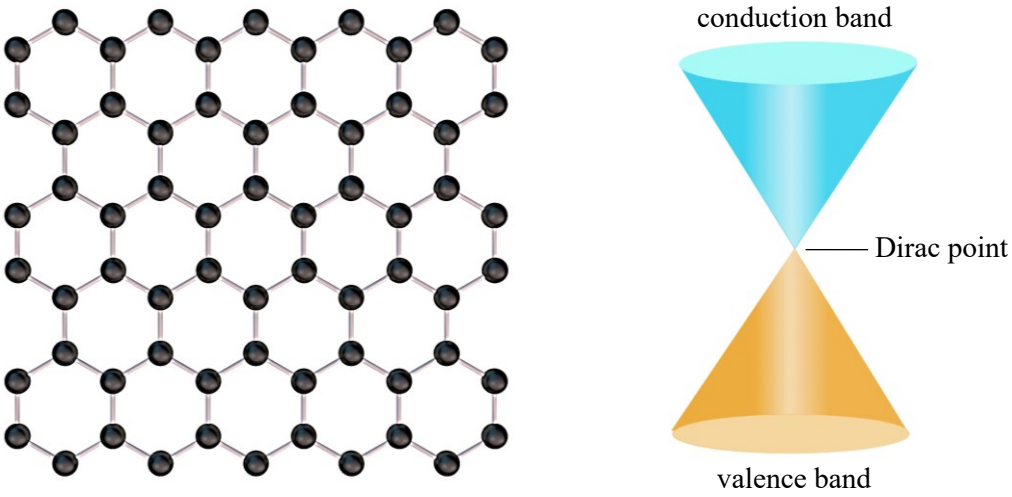

Fig. 4: Hexagonal graphene lattice and corresponding band structure, adapted from [21].

Due to its robust covalent bonding, repetitive structure, low-mass of carbon atom and long-range π conjugation, the graphene exhibits extraordinary mechanical, thermal and electrical properties, such as a high Young's modulus (~1 TPa), fracture strength (~125 GPa), light transmittance (~97.4 %), thermal conductivity (up to 5000 W m^{-1} K^{-1}), high electron mobility (15 000 $cm^2 \cdot V^{-1} \cdot s^{-1}$) and large specific surface area. Graphene monolayer is a zero-band gap semiconductor or semimetal where the conduction band and valence band intersect at the Dirac point (Fig. 4). Here, the electrons behave like massless Dirac fermions moving with a Fermi velocity $v_F \approx 3 \cdot 10^6$ m $\cdot$ s^{-1}. In pure (undoped) graphene, the Fermi energy aligns with the Dirac point [21], [24], [25].

For its unique properties, graphene showed to be a promising material in applications such as electronics (sensors, biosensors, high-frequency transistors, supercapacitors, batteries), inks, lubrication, composites, and graphene-based materials for tissue engineering. Graphene exhibits low toxicity and exceptional biocompatibility under controlled doses. Graphene-based biomaterials have gained recognition for their ability to effectively stimulate stem cell differentiation into nerve cells, as well as their capacity to promote nerve cell proliferation and differentiation [21].

Graphene preparation methods include top-down approaches (mechanical exfoliation, liquid phase exfoliation, electrochemical exfoliation, arc-discharge method) and bottom-up approaches (CVD, Laser-assisted synthesis, Epitaxial growth, CO reduction etc.). CVD approach is described in detail below [21], [25].

2.2 Chemical vapor deposition (CVD)

Chemical vapor deposition (CVD) is an inexpensive deposition method used to produce large-area graphene (and other thin films) by decomposition of volatile hydrocarbon precursors (methane, acetylene) on a metal substrate surface. While the metal substrate primarily serves as a catalyst and lowers the activation energy of the reaction, it also determines the graphene growth mechanism, thus affects the number of layers and quality of graphene. Two major substrates used for CVD of graphene are nickel (Ni) and copper (Cu). The deposition process takes place inside of a CVD chamber. Simplified scheme of such chamber, constructed at Institute of physical engineering (Brno University of technology, Faculty of mechanical engineering), is shown in Fig. 5 [26], [27].

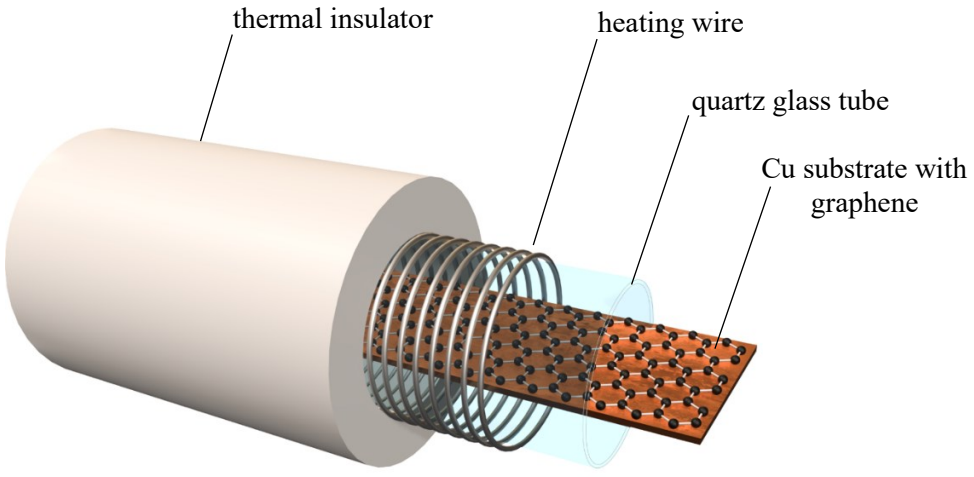

Fig. 5: Simplified scheme of a CVD chamber.

The CVD process is initiated by placing a metal substrate into CVD chamber, which is then evacuated using vacuum pumps (turbomolecular and rotary vane vacuum pumps). In case the polycrystalline Ni substrate is used, thermal annealing in hydrogen atmosphere at a high temperature (approx. 1000 °C) that increases the grain size must follow, as most of the undesired multilayer nucleation occurs at the grain size boundaries. Better-quality graphene can be obtained by using single-crystalline Ni(111) substrate with no grain boundaries. The annealing process also leads to a smoother substrate surface and reduces the number of surface impurities, thus increasing the yield of defect-free graphene on both Ni and Cu substrates. The chamber is then filled with methane. Graphene layer begins to form on the surface of Cu substrate directly after decomposition reaction of the precursor and during cooling. Compared to the Cu, the Ni substrate, however, has relatively high solubility of carbon. The graphene formation process is therefore preceded by carbon diffusion into a substrate, followed by precipitation from the substrate's volume during cooling. The number of formed layers is strongly dependent on the parameters of the cooling process. For this reason, the Cu substrate might appear to be a more suitable CVD catalyst. On the other hand, the lattice mismatch between Ni(111) and graphene is smaller that of Cu and graphene. Therefore, the choice of substrate ultimately depends on the specific requirements of the graphene's application area, as it significantly affects its properties [26], [27].

3 MATERIAL CHARACTERIZATION METHODS

Conventional optical microscopy methods use visible light to obtain magnified image of a sample. The resolution, however, is limited by Abbe diffraction limit which states that to distinguish two objects as individual points, their distance cannot be less than half the wavelength of imaging light. Using the light of wavelength 400 nm (violet), the Abbe diffraction limit restricts the resolution to 200 nm. To obtain more detailed information about the sample, and therefore achieve a higher resolution, a shorter wavelength of electromagnetic waves or accelerated particles must be used [28].

3.1 Scanning electron microscopy (SEM)

Scanning electron microscopy (SEM) is a microscopy technique that uses a focused beam of electrons to obtain information about the sample, such as topography, chemical composition, or crystalline structure [29].

The incident electrons are produced by the electron gun (usually tungsten filament) by thermionic emission, which occurs when the tungsten filament is heated to a high temperature (above 2500 °C). Emitted electron beam is then demagnified by a circular magnetic field produced by electromagnetic condenser lenses. The electron beam scans the specimen in a raster pattern. The surface imaging is then based on the interaction of high-energy electrons with the atoms of the sample. This interaction process produces various signals (Fig. 6) which can be detected, namely backscattered electrons, secondary electrons, auger electrons and x-ray photon emission [29].

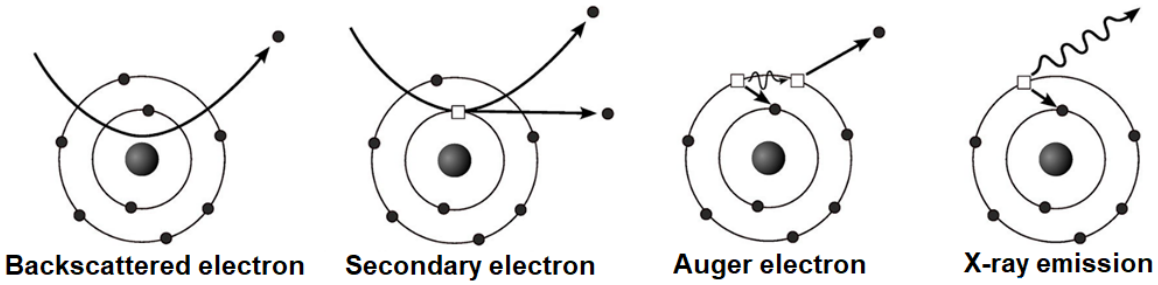

Fig. 6: Interactions between incident electron and the sample adapted from [30].

Backscattered electrons (BSE) are produced when an incident electron approaches the nucleus of an atom close enough to be elastically scattered back through a large angle, thus emerging back on the surface while preserving its high energy. The number of backscattered electrons is depending on the atomic mass. Therefore, BSE image contrast provides

information about chemical compositional differences. This applies especially to materials with significant differences in atomic number [29]

Secondary electrons (SE) are created when incident electron ejects weakly bound electrons out of their orbits around an atom. Secondary electrons emerge from a near-surface layer of a sample and their energy does not exceed 50 eV, thus making them useful for examination of the sample surface, as they primarily provide topographic information [29].

When an inner-shell electron is ejected by incident beam, a higher-energy outer-shell electron fills the vacancy. During this process, the energy difference is either released in a form of an X-ray photon, or transferred to another electron, causing its emission as an low-energy Auger electron. Analysis of Auger electrons and their energies provides information about elemental composition of the sample [29].

Considering the de Broglie wavelength of an electron (under an acceleration voltage of 10 kV) and the Abbe diffraction limit for electron microscopy, the maximal theoretically obtainable resolution is on the order of picometers. Due to the effect of spherical and chromatic aberrations in electromagnetic lenses, causing the distortion of an electron beam, the actual maximal obtainable resolution is in the order of nanometres [31].

3.2 Atomic force microscopy (AFM)

Atomic force microcopy (AFM) is a microscopy method belonging into a group of Scanning probe microscopy (SPM). Using a physical probe to scan the specimen, these methods can measure variety of local properties, such surface topography, electrical forces, potential, conductivity or magnetic forces [32].

The probe consists of a sharp tip on a cantilever attached to a holder. As the probe scans the surface, a laser beam is reflected off a cantilever into a four-segment photodetector. The contact of probe with sample surface during scanning causes the bending of cantilever and therefore the deflection of the beam. The differences in reflected laser beam indicated by the segments of photodetector enables the surface topography imaging. Precise movements of the probe are facilitated by piezoelectric ceramics [32].

AFM maps a surface topography through a detection of force interaction between atoms of a sample surface and probe tip, causing the cantilever deflection. These interatomic forces are of electromagnetic nature, namely the van der Waals attractive forces and short-range Pauli repulsive forces. The interaction of both gives rise to a Lennard-Jones potential

(L–J potential in Fig. 7), which is an approximate model for the interaction between two neutral atoms, originally developed for noble gases:

$$U(r) = \varepsilon\left[\left(\frac{r_0}{r}\right)^{12} - \left(\frac{r_0}{r}\right)^{6}\right] \tag{6}$$

where *U(r)* is the L–J potential, ε is the specific L–J parameter, r_0 is the interatomic distance at which the potential becomes a minimum and *r* is the distance between two interacting particles [32].

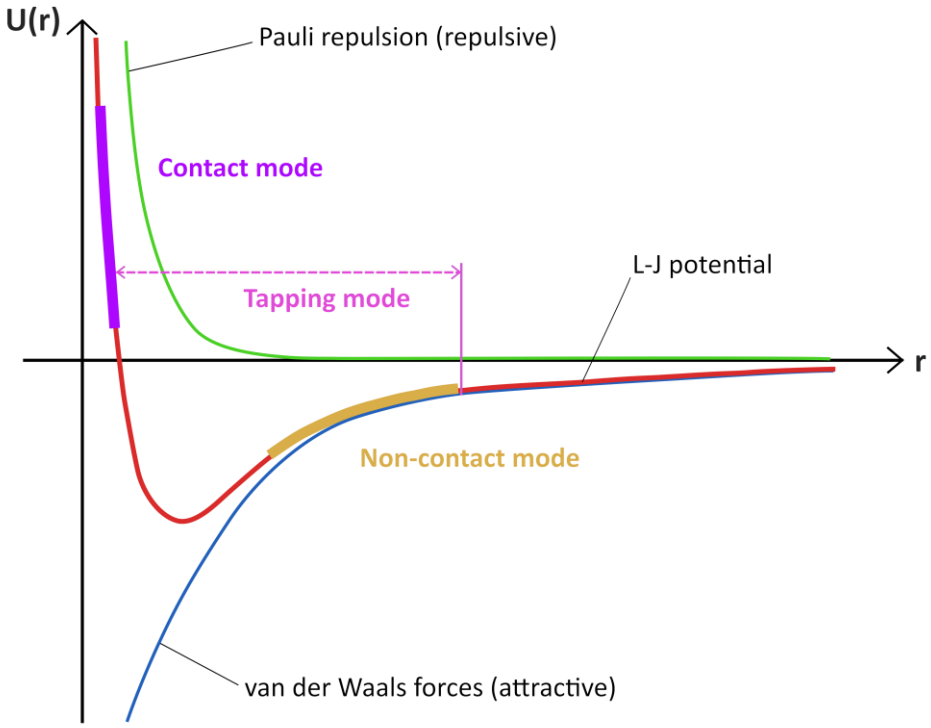

Fig. 7: Lennard-Jones potential as a function of the particle distance, adapted from [33].

Based on the tip-surface distance during the measurement, the probe can operate in different regimes. In the contact mode, the Coulomb repulsive forces are dominant, as the distance between probe tip and sample is short and the tip is dragged across the surface. The possibility of sample damage from the tip led to the development of the non-contact mode, where the probe tip operates at a larger distance of 1-10 nm from the sample surface. The cantilever is set to oscillate at its resonant frequency. Selected amplitude value must prevent the tip from contacting the sample surface [32]. The combination of both modes is the tapping mode, where the cantilever is oscillating up and down with amplitude value allowing the tip to touch the sample surface periodically. Imaging modes mentioned above can be seen in Fig. 7.

The AFM can achieve resolutions high enough to visualize sample properties in the order of nanometers, the actual resolution however depends on factors such size and shape of the probe tip or stiffness of the cantilever [32].

3.3 Raman spectroscopy

Raman spectroscopy is a non-destructive spectroscopic method used to examine the chemical composition of a sample by determining the vibrational modes of molecules through scattered light analysis [34].

The interaction of electromagnetic radiation with a molecule induces a virtual vibrational state. The incident photon of electromagnetic radiation induces a short-lived distortion in the electron cloud of a molecule, thus inducing a temporarily polarized dipole. In vast majority of cases, the oscillation frequency of the induced dipole is the same as the frequency of field of the incident light, thus no shift in the frequency of a reemitted photon occurs. This process, during which the wavelength of the incident photon is equal to the scattered one, is called Rayleigh scattering (elastic scattering) [34], [35].

In some cases, the oscillation frequency of the induced dipole is different from the frequency of an incident photon due to the change in the vibrational or rotational state of the molecule, resulting in the shift at the frequency of reemitted photon. This phenomenon, which is referred to as the Raman effect (Raman scattering, inelastic scattering), occurs very rarely – only one incident photon in 10^7 is inelastically scattered [34], [35].

The energy of emitted photons created during the Raman effect can be both decreased and increased compared to the energy of incident light. If the scattering process leads to an excited vibrational state of the ground state of a molecule, the energy of a scattered photon is lower than the energy of incident photons. On the other hand, if the molecule is already vibrationally excited, the scattered photon is energetically higher than the energy of an incident photon, as the molecule returns to its ground state. These phenomena are referred to as Raman Stokes and Raman anti-Stokes scattering and in both cases, the energies of scattered photons are proportional to the energies of vibrational levels of the molecule. These energy transitions (including Rayleigh scattering) are shown in Fig. 8. The energy difference between incident and scattered photon is called Raman shift [34], [35].

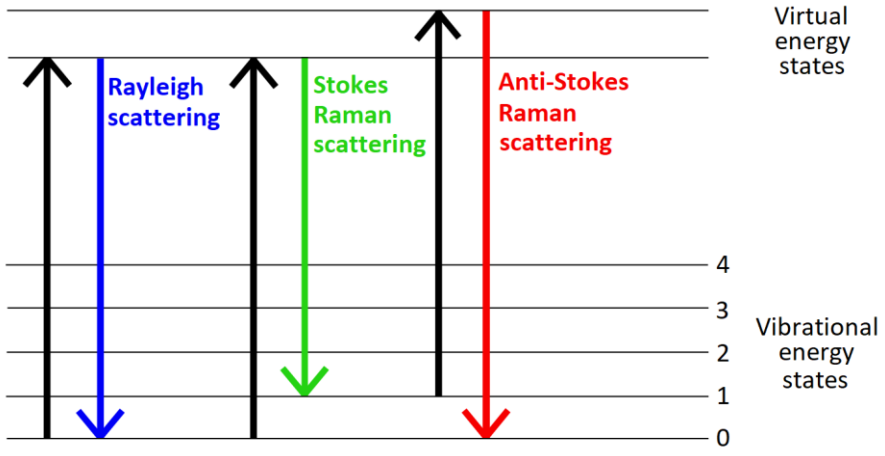

Fig. 8: Diagram of molecule's energy transitions in Raman spectroscopy. Adapted from [36].

Energy E of elastically scattered photon can be expressed as:

$$E = h\nu_i \tag{7}$$

where h is the Planck constant and ν_i is the frequency of an incident photon. Energy of inelastically scattered photon is equal to:

$$E = h(\nu_i \pm \nu_v) \tag{8}$$

where ν_v is frequency of vibrational mode, + is for Stokes Raman scattering and – is for anti-Stokes Raman scattering [36].

Raman spectrometers use a laser as a source of monochromatic light. The scattered light from the sample is collected by the optics and led through interferometer or monochromator to the detector. Various monochromators (laser line filters, edge filters, notch filters) are used to filter out fluorescence emission, Rayleigh line (incident laser line) and Anti-Stokes lines as their signal is weaker in intensity compared to Raman Stokes lines [37].

3.4 Contact angle

Interactions between molecules at the interface of two phases differ from those within the bulk phase. This contrast is particularly evident in *l/g* interfaces, where molecules near the surface of the liquid have fewer neighbouring molecules compared to those in the bulk. When a molecule moves from the bulk phase to the surface layer, its energy increases. The work dW required to create a new surface is equal to:

$$dW = \gamma \cdot dA \tag{9}$$

where dA is the area of the newly created interface and the constant γ represents the surface energy ($J \cdot m^{-2}$). The surface energy is alternatively called the surface tension ($N \cdot m^{-1}$), since it can also be expressed as Eq. 11: [38].

$$\gamma = \frac{F}{L} \tag{10}$$

where F is the force acting per unit length L along the surface of the liquid, perpendicular to an imaginary line on the surface [38].

If a liquid drop is placed on a solid surface, the liquid spreads over the surface in a continuous layer if the surface energy of the solid γ_{sg} is greater than the sum of the surface energy of the liquid γ_{lg} and the energy of the solid-liquid interface γ_{sl}. On the other hand, if the γ_{sg} is smaller than the sum of γ_{lg} and γ_{sg}, the liquid drop will assume an equilibrium shape on the surface of the solid, characterized by a wetting angle (contact angle) θ. Contact angle θ is the angle formed at the point where the solid-liquid interface intersects the tangent line to the surface of the liquid droplet. The equilibrium condition, which considers the balance of interfacial tensions, is expressed by Young's equation [38].

$$\gamma_{sg} = \gamma_{sl} + \gamma_{lg} \cdot \cos\theta \tag{11}$$

Fig. 9 illustrates a water droplet on a solid surface exhibiting different contact angle. In case of complete wetting (a) of the surface, the contact angle is zero. If $0° < \theta < 90°$ (b), the wetted surface is referred to as hydrophilic (in case the wetting liquid is water). If $90° < \theta < 180°$ (c), the wetted surface is referred to as hydrophobic. The $\theta = 180°$ corresponds to a superhydrophobic surface (d).

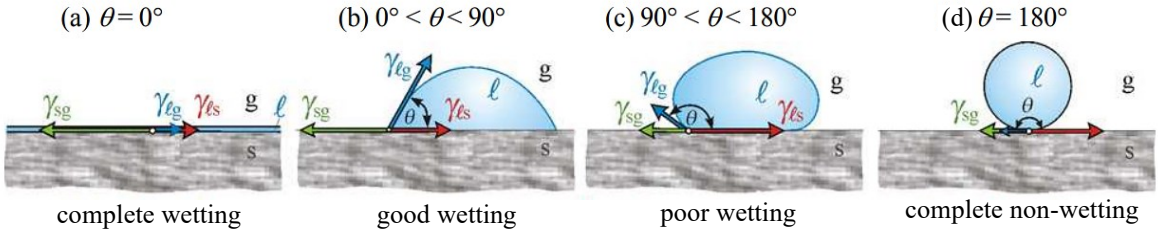

Fig. 9: Water droplet on the surface of a solid. Adapted from [38].

Contact angle can be measured using various techniques, one of which is the direct measurement method using the sessile drop technique. In this method, a droplet of the studied liquid is placed on a solid surface and the droplet shape together with the contact angle value is determined with the aid of a goniometer and software [38].

Contact angle therefore provides information about the surface energy of a system and related adhesion properties. For polymer materials, various surface modification techniques, including breath figures, phase separation, plasma treatment or corona discharge, are commonly utilized to modify the surface properties, i. e. contact angle values and surface energy. In the case of biomedical applications, polymer surfaces exhibiting water contact angles ranging from 40° to 70° effectively promote cell adhesion [39].

II. ANALYSIS

4 MATERIALS AND METHODS

This section contains a detailed description of the experimental procedures performed, along with details regarding the measuring instruments and materials used.

4.1 Materials and reagents

Polycaprolactone (PCL) pellets (Sigma-Aldrich Ltd., average Mn 80 kDa) were dissolved in tetrahydrofuran (THF; 99.8 %; RCI Labscan Ltd) which served as a good solvent. 2-ethoxyethanol (2-EE; p. a., Sigma-Aldrich Ltd.) was added to the prepared PCL + THF solution as a poor solvent to induce phase separation upon dosing. Samples were rinsed in ultra-pure distilled water obtained from Direct-Q® 3 UV water purification system.

Iron(III) nitrate nonahydrate (98 %), hydrochloric acid (HCl; 36%) and other chemicals utilized in wet transfer of graphene were bought at Sigma-Aldrich Ltd.

For MTT assay and cell proliferation, mouse embryonic fibroblast cell line was utilized (ECACC 93061524, England), together with the ATCC–formulated Dulbecco's Modified Eagle's Medium (Biosera, France) containing 10% of calf serum (BioSera, France) and 100 U ml^{-1} Penicillin/Streptomycin (Biosera, France).

4.2 Sample preparation and purification

Polymer samples of porous PCL structure were prepared by deposition of PCL solution and subsequent modification by time-sequenced dosing of mixed solvents. For a deposition of PCL solution and mixed solvents, a TSSC device (Time Sequenced Spin Coater) developed at the Department of Physics and Materials Engineering in Thomas Bata University in Zlín was used (see Fig. 10 a).

Also, based on the research activities of the Department of Physics and Materials Engineering in Thomas Bata University in Zlín, the synthesis conditions (i. e. spin-coating parameters, as well as the proportions of polymer and volumes of solvents used) of three different PCL surface types (A, B and C) were proposed. These can be seen on the following page in Table 1.

Samples were prepared under different humidity conditions and within a temperature range of 21 to 23 °C.

Table 1: Synthesis conditions regarding the PCL porous samples preparation

Surface type (-)	Dosing mixture (-)	Rotation speed (RPM)	Rotation time (s)	Dosed volume (ml)	Dosing speed (RPM)	Number of doses (-)	Dosing delay (s)
A	1.978 g PCL 20 ml THF (10.0 wt%)	0	0	2.50	80	1	0
B	1.978 g PCL 20 ml THF 26 ml 2-EE (4.5 wt%)	1200	60	0.48	80	10	5
C	10 ml THF 0.1 ml H_2O	1500	120	0.30	80	3	5

In this work, the proposed synthesis conditions kept unchanged. The experimental work involved altering only the humidity conditions, as its impact on the preparation of porous polymer surfaces has not been yet extensively studied. For this purpose, a simple controlled atmosphere chamber was constructed (Fig. 10 b):

Fig. 10: TSSC - Time Sequenced Spin Coater (a), constructed atmosphere chamber (b).

4.2.1 Preparation of porous polycaprolactone surfaces

The initial stage in producing PCL involved the preparation of PCL solutions. A different solution had to prepared for each surface type. It is important to emphasize that surfaces B and C were not individually prepared, instead, they were obtained through surface modification (phase separation) of samples of the preceding type: A → B → C. Therefore, the initial surface structure A was not prepared using phase separation (apart from surface structure B and C), instead it was obtained simply through solidification process. The experimental procedure followed during PCL samples preparation is illustrated in Fig. 11:

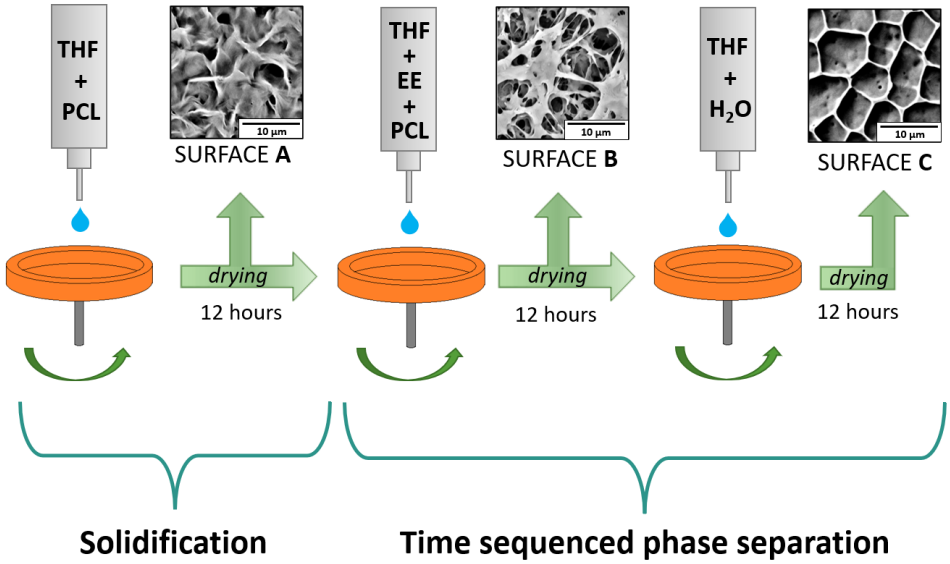

Fig. 11: Illustration of the experimental procedure of porous PCL samples preparation.

For the preparation of PCL surface type A, a solution was made by dissolving 1.978 g PCL in 20 ml THF (good solvent). The dissolution of the PCL pellets was completed within 4 hours. However, viscous polymer solution contained both semi-transparent and non-transparent impurities (up to 1 mm) of undissolved clumps of polymer chains. Even after extending the dissolution time by an additional 6 hours (10 hours total), these impurities persisted. The presence of these undesired impurities was observed even after the preparation (dosing) of each surface type, as depicted in Fig. 13. Therefore, the polymer solution was filtered using a glass fritted funnel of S1 type (porosity 100 – 160 μm), resulting in fully transparent, impurity-free polymer solution (Fig. 12). It was later found that similar outcome could also be achieved by placing the beaker with polymer solution to a mildly warm water bath (approximately 30 °C) for less than 10 minutes. As a result, the dissolution time of each

polymer solution (for PCL surfaces type A and B preparation) was set to 10 hours and each polymer solution was also filtered.

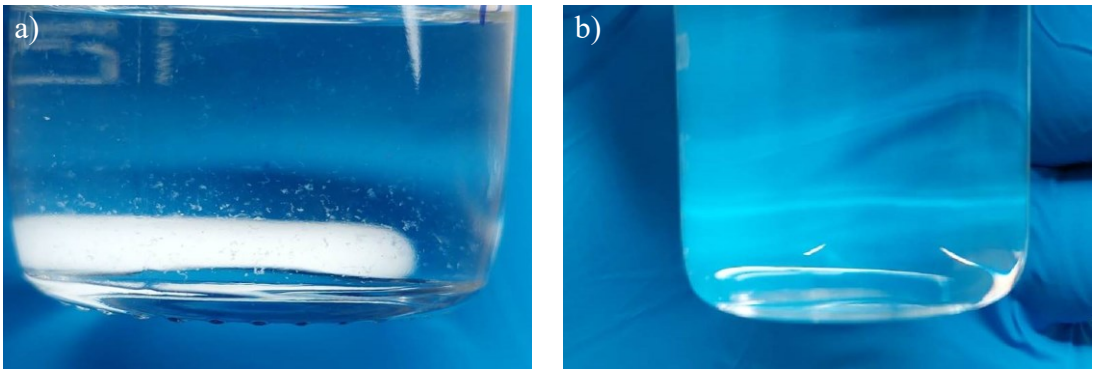

Fig. 12: PCL + THF solution after 10 hours of dissolution, before (a) and after (b) filtering using glass fritted funnel of S1 type (porosity 100 – 160 μm).

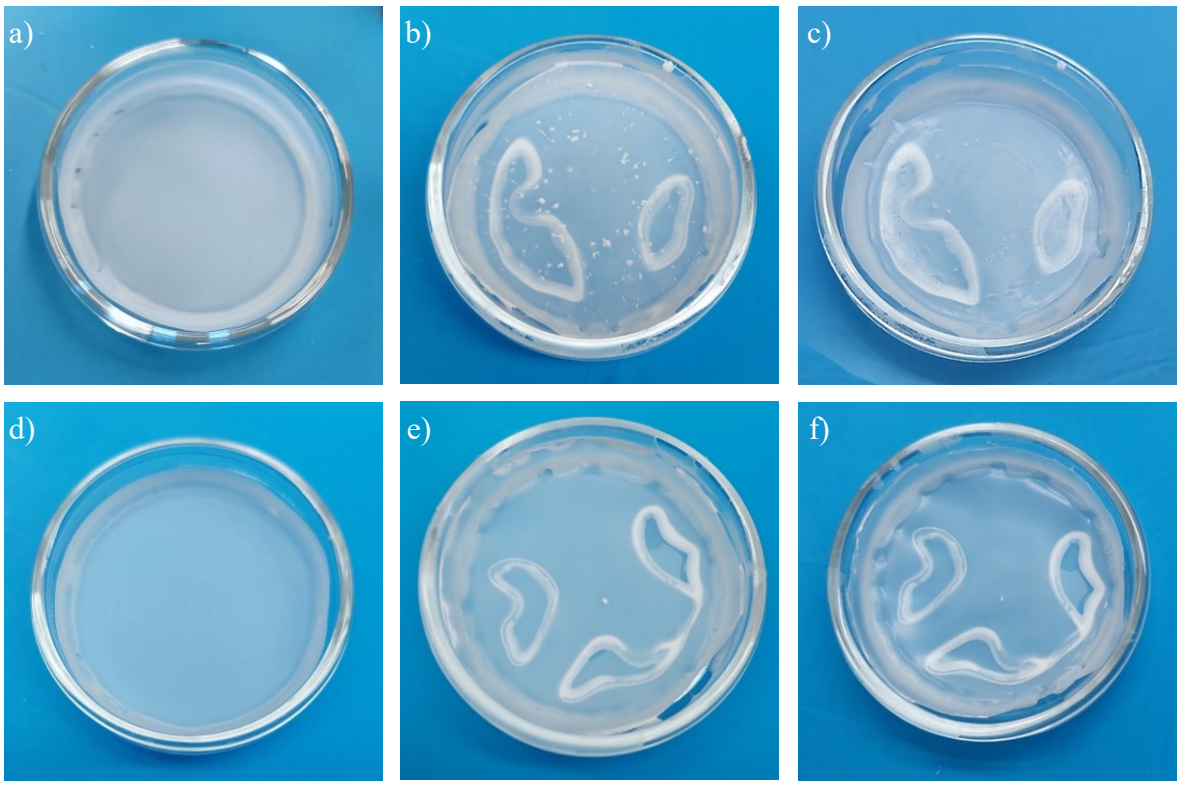

Fig. 13: Set of PCL surface type A (a, d), B (b, e) and C (c, f) samples prepared from unfiltered solution (a, b, c) and filtered solution (d, e, f).

Filtered solution was drawn into a glass syringe (volume 20 ml) and placed into a spin-coater. A glass Petri dish with a diameter of 35 mm was positioned underneath the needle in spin-coater. The spin-coater was enclosed within a controlled atmosphere chamber, and once the desired humidity conditions were achieved, the synthesis sequence (according to Table 1) was initiated. After completing the dosing sequence and rotation, the Petri dish with

the PCL sample was covered with a larger diameter Petri dish and transferred to a desiccator. Not only does the Petri dish cover protect the sample during transfer, but its presence in desiccator also prevents the PCL sample from curling, which would occur due to the volatility and rapid evaporation of remaining solvent. The samples were subjected to a dry air follow within a desiccator for a minimum drying period of 12 hours.

In general, the experimental procedure described in the paragraph above can be applied to the preparation of all three PCL surface types. In the case of preparation PCL surface type B structure, 26 ml of 2-EE (poor solvent) were slowly pipetted into the solution after 10 hours of dissolution time. The solution for the PCL surface type C preparation was prepared immediately prior to the dosing procedure. Regarding the PCL surface type B and C preparation, it is evident that both type B (Fig. 13 b, e) and type C (Fig. 13 c, f) samples exhibit the presence of distinct white lines arranged in various formations. The presence of these lines is a direct consequence of the synthesis conditions, specifically the insufficient rotation time during the preparation of PCL surface type B (see Table 1). During the rotation process, the solvent mixture is being accumulated along the inner edge of the Petri dish (and PCL sample) due to centrifugal force. As the rotation is terminated before the complete evaporation of the solvent mixture, the solvent mixture tends to distribute evenly across the entire sample area. Due to minor irregularities in the sample's flatness, certain areas of the sample make direct contact with the Petri dish, while others are slightly elevated. The areas where the sample touches the dish directly are the entry points for the solvent mixture. Although this does not cause the destruction of generated porous structure, these lines or band-like areas may exhibit signs of decreased porosity.

All PCL surface types (A, B and C) were prepared under four different humidity conditions. Low relative humidity values (RHs) were achieved by using dry air flow (silicon tube, ⌀ 0.7 mm), whereas high RHs were accomplished by humidifying the incoming air through the apparatus with water (distilled water at a room temperature). Induced humidity conditions, including the corresponding air-flow values, are outlined in the following table:

Table 2: RHs with corresponding air speed and air flow values.

	RH = 15 %	RH = 35 %	RH = 50 %	RH = 70 %
Air speed (m · s)	5.0	0.21	5.98	1.28
Air flow ($cm^3 \cdot s^{-1}$)	1.92	0.08	2.3	0.49

The RHs and airflow values were measured using a multifunction multimeter Testo 435-2 (TESTO AG). Finally, it should be noted that based on the SEM observations of each prepared structure, each subsequent surface type was prepared using the best sample of the previous structure type, which was mostly obtained at RH = 50 % and RH = 70 % (See RESULTRS – SEM).

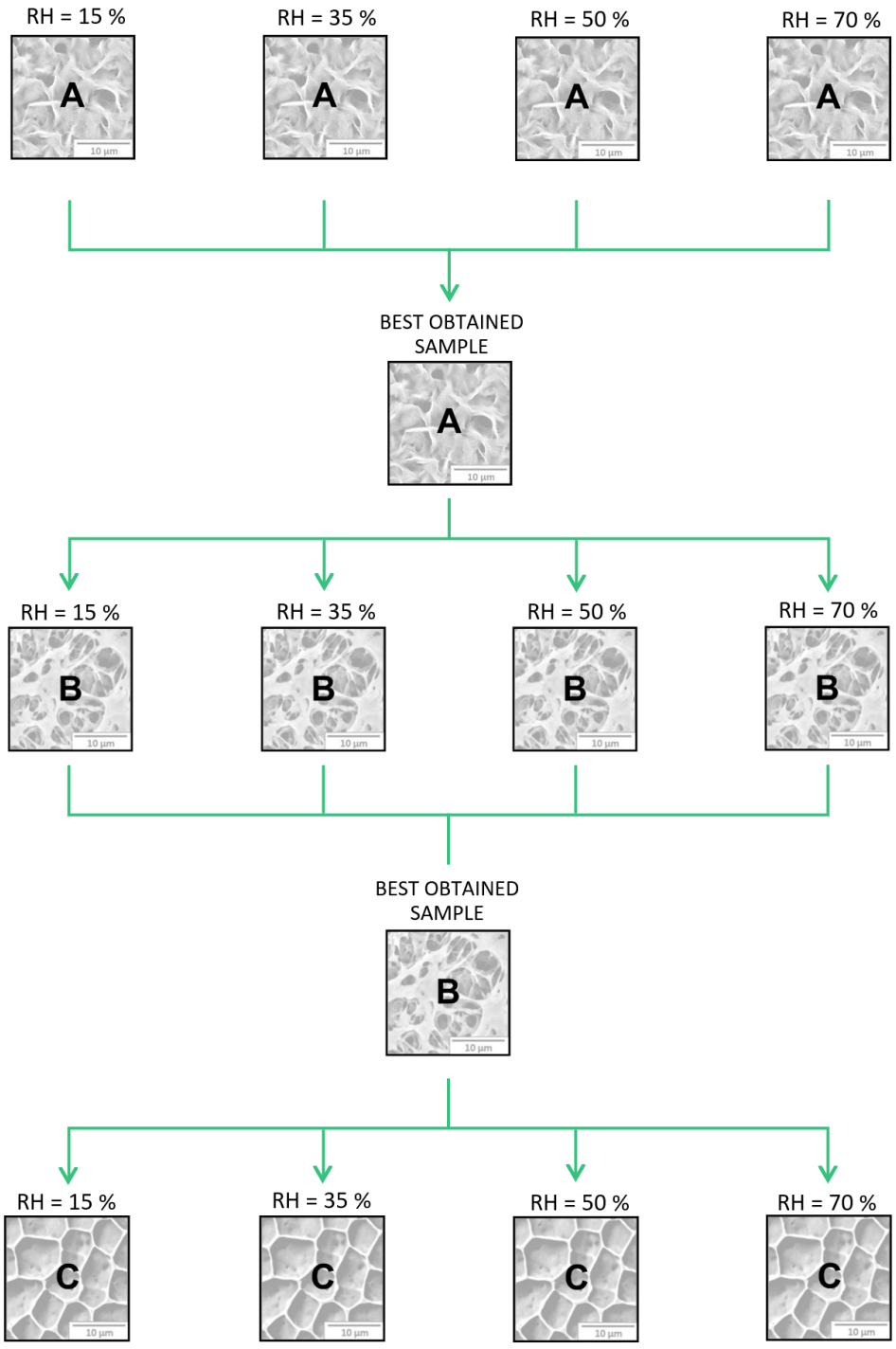

Fig. 14: Scheme of porous PCL surfaces preparation.

From this point onward, only PCL surface type C samples will be subjected to all subsequent experimental procedures, since it can be considered as the final structure with the best-defined porosity and also due to the significant number of experiments required to be conducted on all PCL surface types.

4.2.2 Purification of porous polycaprolactone surfaces

The goal of the purification process is to achieve maximum sample purity, as the potentially present residues of toxic organic solvents in PCL film can have negative impact on cell viability. This was primarily achieved by rinsing of PCL type C films in a large container filled with ultra-pure distilled water (obtained from Direct-Q® 3 UV water purification system) and clean stirrer magnet on the bottom. To ensure the surface porous structure would remain intact, a mesh was placed in the container to avoid contact of polymer film and stirrer magnet. The container was then placed on a magnetic stirrer and set to 300 RPM. After 24 hours of rinsing, the samples were removed from the container and were left to dry in a desiccator under dry air flow.

To achieve even higher purity, the samples were subjected to vacuum during freeze drying process in Freeze dryer Alpha 2-4 LSCbasic (Martin Christ). The freeze-drying process consists of two stages. During stage I, the pressure was reduced to 0.06 mbar and temperature was decreased to -85 °C. After 30 hours, the pressure was reduced to 0.001 mbar. Stage II lasted 45 hours and temperature remained the same.

4.2.3 Graphene transfer

The process of graphene transfer onto the porous PCL surface of type C involved following steps: spin coating of PMMA on a copper foil (Cu) with CVD-grown graphene, oxygen plasma etching of Cu and a complete Cu removal using chemical etching.

PMMA 50 (AR-P 639.04) was spin-coated at 2200 RPM and annealed at 150 °C for 5 minutes. The purpose of the approx. 1.5 μm thin PMMA layer is to minimalize the risk of damage due to mechanical stress that can occur during the transfer process. As both sides of the copper substrate get covered with graphene during CVD process, the bottom side of the substrate must be removed to ensure that only one graphene layer would be transferred. This was achieved by oxygen plasma etching (deep reactive ion etching) using PlasmaPro 100 DRIE (Oxford Instruments).

The last step during which the Cu foil was dissolved in etchant and graphene was transferred to a target substrate is commonly referred to as wet transfer. This process is schematically shown in Fig. 15 below:

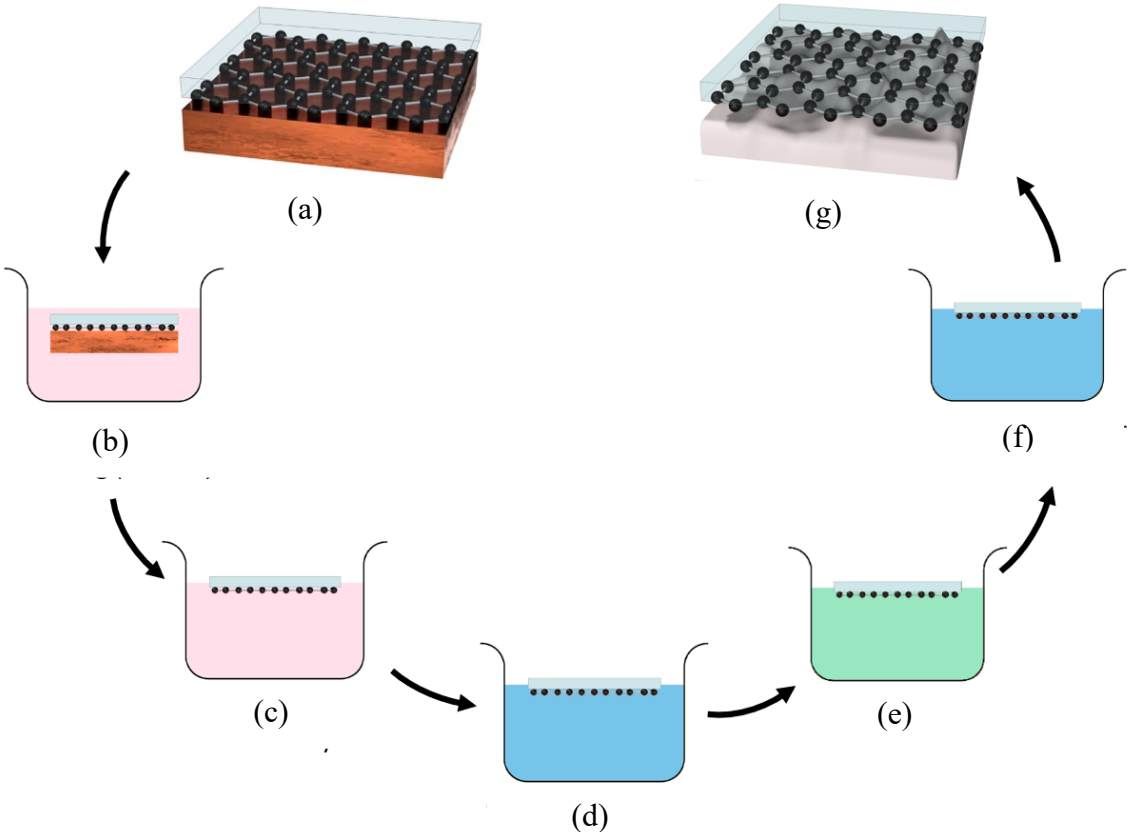

Fig. 15: Wet transfer process of CVD-grown graphene coated with PMMA layer: (a) Cu-Gr-PMMA, (b) 1M $Fe(NO_3)_3 \cdot 9H_2O$, (c) floating Gr-PMMA layer, (d) deionized water, (e) 5% HCl (5 minutes), (f) deionized water, (g) porous PCL-Gr-PMMA.

The Cu foil with graphene and spin-coated PMMA (a) was placed into a beaker (b) with 1M iron(III) nitrate nonahydrate solution in course of 4 hours, resulting in the dissolution of the Cu foil (c). To remove the majority of residual impurities of copper, iron(III) nitrate crystals and other contaminants deposited during CVD process, the floating Gr-PMMA layer was lifted with tweezers and transferred to beaker with deionized water (d), followed by bath in 5% HCl solution (e). After one last rinsing in deionized water (f), the floating Gr-PMMA layer was transferred to the porous PCL sample (g). The PMMA layer was then removed by rinsing in acetone for 1.5 hours.

In total, six PCL-Gr-PMMA samples were prepared – two were further studied by Raman spectroscopy (one with PMMA layer still present) and four samples were later used for biocompatibility tests.

4.3 Sample analysis methods

4.3.1 SEM

The topography of prepared PCL surfaces was observed by scanning electron microscope Phenom G2 PRO with an acceleration voltage of 10 kV. For SEM examination, a 0.5 x 0.5 cm area from between the edge and the centre of the sample was cut from each PCL film. Due to the non-conductive nature of the PCL, an ultra-thin metal layer was deposited on the sample during the process of sputtering (45 seconds, 18 mA, sputter coater SC7620 Mini with Au/Pd target) to prevent the accumulation of charge. Obtained images were further processed in the software ImageJ, which was also used for the pore size distribution analysis.

SEM images presented in section 5. RESULTS are 6000x magnified. For various magnification values, see Appendix II: SEM images of PCL surfaces (type A, B, C), four different magnifications.

4.3.2 Contact angle measurement

The contact angle of water on prepared PCL surfaces was measured using the Drop Shape Analyzer – DSA30 (Krüss). The mean value of the water contact angle was determined from 10 measurements for each surface type (A, B, and C prepared under 4 different humidity conditions), after their statistical processing. Dispensed water droplets were 3 µl in volume.

4.3.3 AFM

The surface morphology of sample C was measured by atomic force microscope NTEGRA Prima, using a silicon n-type probe with resonance frequency of 150 kHz and spring constant 5.5 $N \cdot m^{-1}$. Two areas of 50 x 50 µm and 5 x 5 µm were scanned with resolution of 512 x 512 pixels and scan rates of 0.5 Hz and 0.7 Hz. Measurements were performed at room temperature. Obtained data were processed using Gwyddion software.

4.3.4 Raman spectroscopy

The graphene monolayer transferred to the porous PCL surface was detected using Confocal Raman Imaging microscope aplha3000 R (WITec). The samples were investigated before and after the PMMA layer removal using depth scanning (*x* or *y*-axis constant) or large area scanning (*z*-axis constant). In the case of a sample with a PMMA layer present, a depth scanning of a 50 x 50 µm area was successfully performed using laser excitation wavelength of 532 nm and laser power of 10 mW. With 40 points per line and 40 lines per image, the

scanning speed was 40 second per line. For a sample with PMMA layer removed, a large area scanning of 15 x 15 μm was performed. The laser parameters, as well as scanning speed, remained the same. Acquired data were analysed by WITec Suite FIVE software.

4.3.5 MTT assay and cell proliferation

MTT assay was conducted via direct contact approach (extract exposure approach was not chosen due to small number of samples available). Embryonic mouse fibroblast cell line NIH/3T3 cells were first cultivated for 24 hours in a 24-well plate dish at a concentration of 2×10^5 cells per ml in a culture medium (the ATCC–formulated Dulbecco's Modified Eagle's Medium – Biosera, France) at 37°C in 5% CO_2 humidified air. After 24 hours, PCL surface type C samples (UV-stertilized) were positioned with the intended side (i. e. side with porous structure and also with graphene) facing downwards onto the surface of the culture medium. After the addition of PCL samples, the cell culturing process was continued for an additional 24 hours. The PCL samples were then transferred to a separate plate, followed by the addition of MTT solution at a concentration of 0.5 mg/ml. Further analysis was not viable (see RESULTS – MTT assay and cell proliferation).

For cell proliferation assessment, embryonic mouse fibroblast cell line NIH/3T3 cells were cultivated in a culture medium (the ATCC–formulated Dulbecco's Modified Eagle's Medium – Biosera, France) at 37°C in 5% CO_2 humidified air. Cells were seeded on the tested samples (UV-sterilized PCL surface type C samples with and without graphene, both sides, 20 min). After 48 hours of proliferation, cells (stained with Hoechst and ActinGreen™ dye) were observed by fluorescence microscope Olympus IX81.

5 RESULTS

In this section, the results of various measurements and experiments will be presented.

5.1 SEM

Detailed surface structure of prepared samples can be seen in Fig. 16. PCL surface type A is covered with conical, sharp-peaked formations with signs of porosity. The type B surface exhibits an increase in porosity, as well as an increase in pore depth. Porous areas are here separated by non-porous bands, whereas in surface type C the pores, which are approximately spherical in shape, are separated by a sharp thin boundary, thus porosity predominates over the non-porous regions. The SEM image also shows that this type of surface has small pores inside larger ones. SEM images of individual PCL surface types, prepared under different humidity conditions, are shown in following pages.

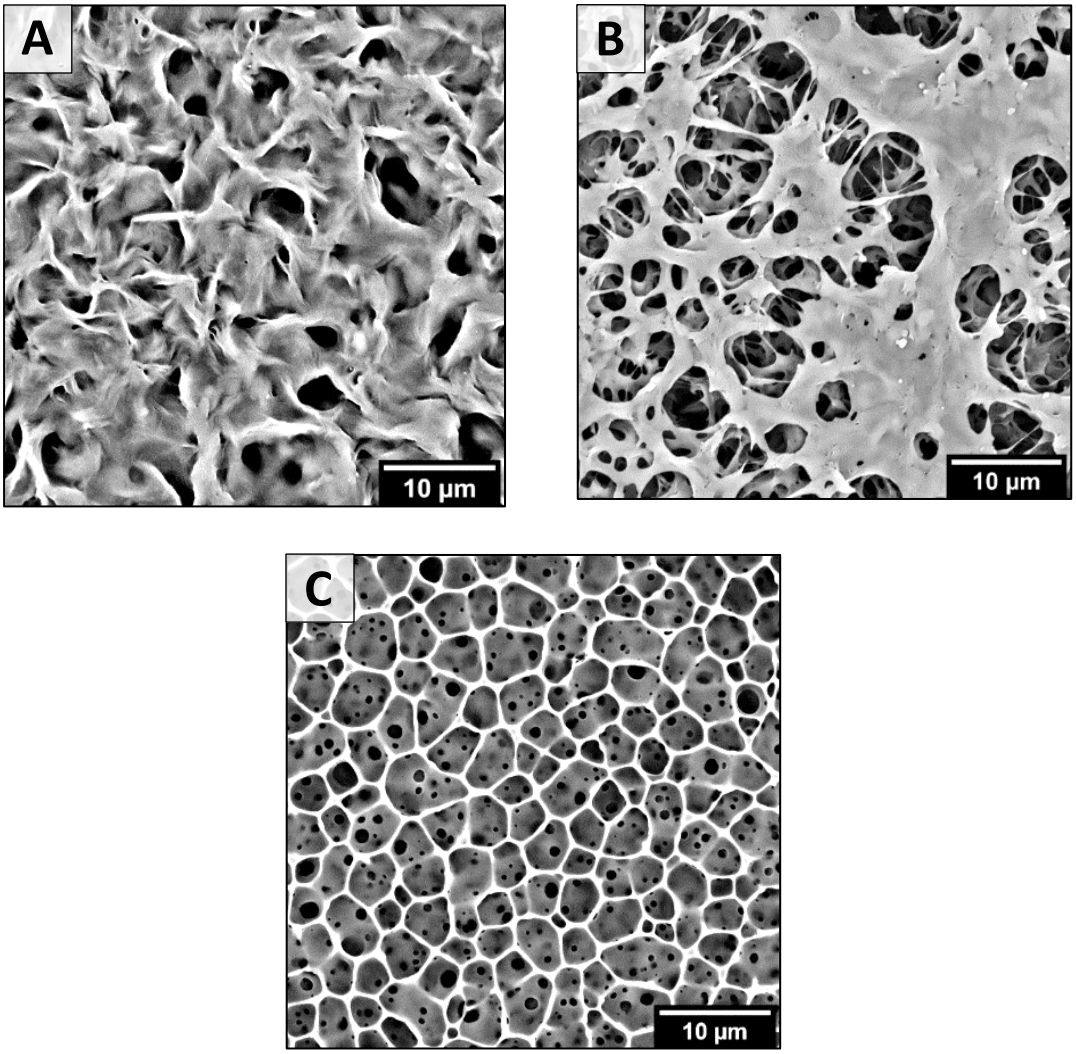

Fig. 16: SEM results of a PCL surface preparation by solidification process (surface A) and phase separation induced by time-sequenced dosing of mixed solvent (surface B, C).

5.1.1 Surface type A

Fig. 17 shows the SEM results of the type A PCL surfaces prepared under four different relative humidity values (RHs). The obtained images exhibit no significant differences in the surface morphology related to the humidity during sample preparation, since the surface structure was formed in the desiccator under a dry airflow during the solidification process over the course of a few hours.

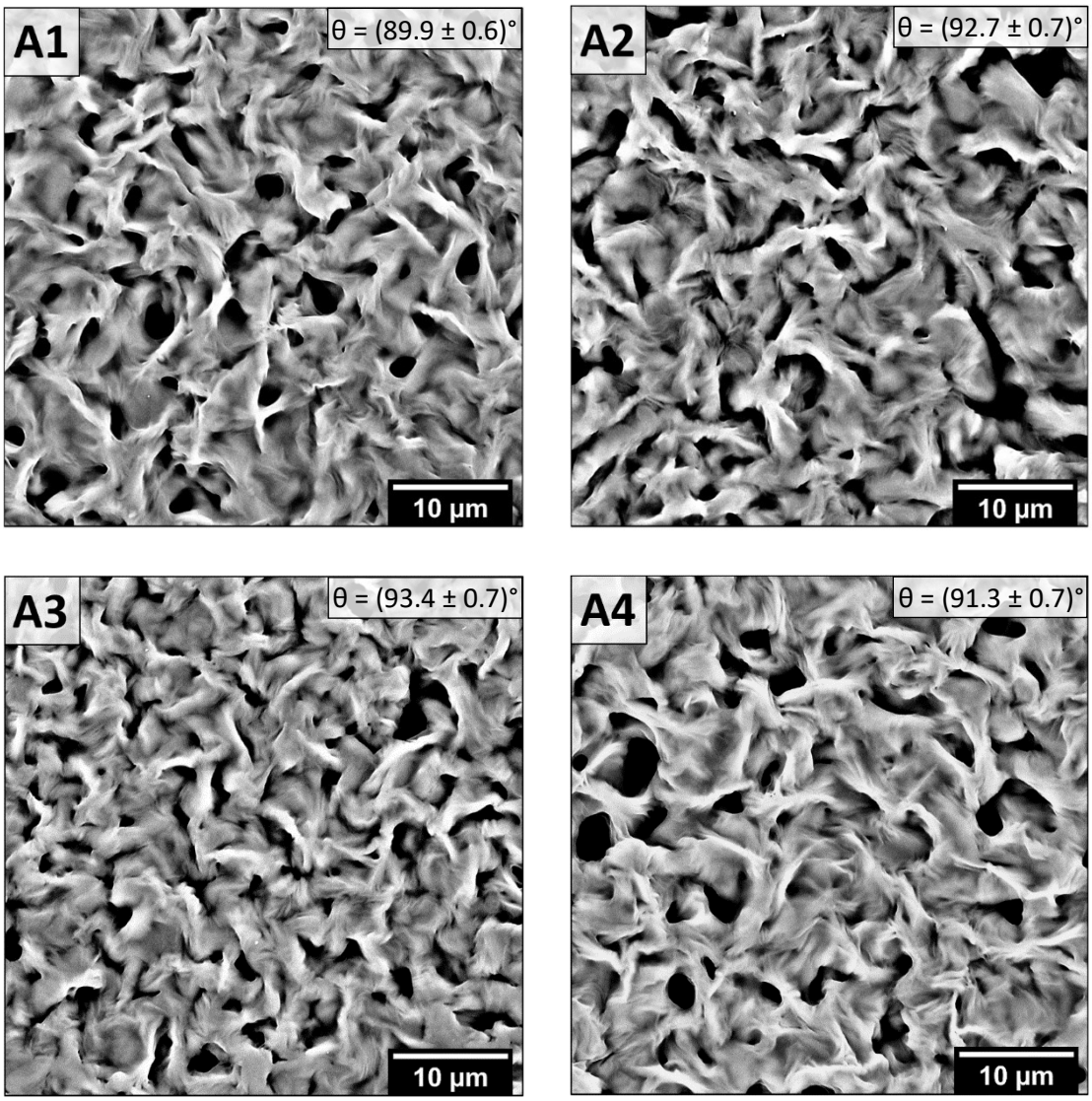

Fig. 17: SEM results of type A PCL surfaces prepared under different RHs: 15 % (A1), 35 % (A2), 50 % (A3) and 70 % (A4). Samples were prepared by dosing ***1x 2.5 ml of 10% PCL in THF.***

5.1.2 Surface type B

The surface modification results of PCL surface type A by phase separation induced by time-sequenced dosing of mixed solvent with dissolved PCL showed high humidity dependence. As is evident in Fig. 18, the ideal surface texturization can be observed at humidity values reaching 50 % and 70 % (B3 and B4). While the B2 surface (RH = 35 %) image indicates that the surface modification process, i. e. phase separation occurred to certain degree, but was prematurely terminated, B1 surface image with remnants of original surface structure (type A) suggests the evaporation rate of dosed solvent mixture was too high for a phase separation to occur.

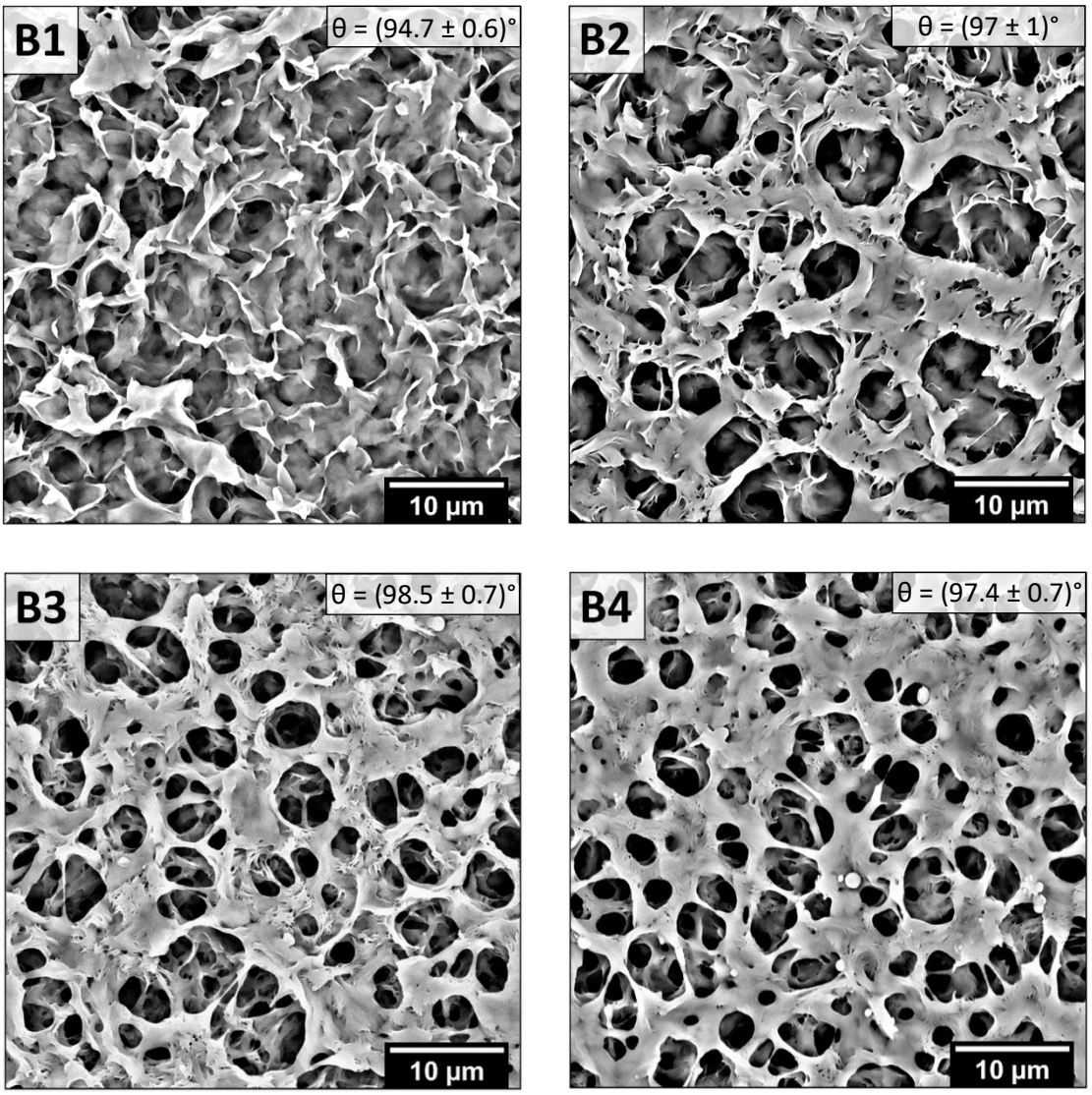

Fig. 18: SEM results of type B PCL surfaces prepared under different RHs: 15 % (B1), 35 % (B2), 50 % (B3) and 70 % (B4). Samples were prepared by dosing ***10 x 0.48 ml of 4.5% PCL in THF + 2-EE.***

5.1.3 Surface type C

SEM results of mixed solvent dosing (without dissolved PCL) on a PCL surfaces of type B (prepared at RH = 50 %) provided a similar pattern of humidity dependence as in the case of surface type B preparation. It is also evident (in Fig. 19) that the pore size grows with increasing humidity, giving the water droplets (poor solvent) time to aggregate and grow. However, under low humidity conditions (RH = 15%), this surface treatment leads to the destruction of all porosity on the sample surface due to rapid evaporation of THF. Smaller non-porous areas can also be present in samples prepared at RH = 35 %.

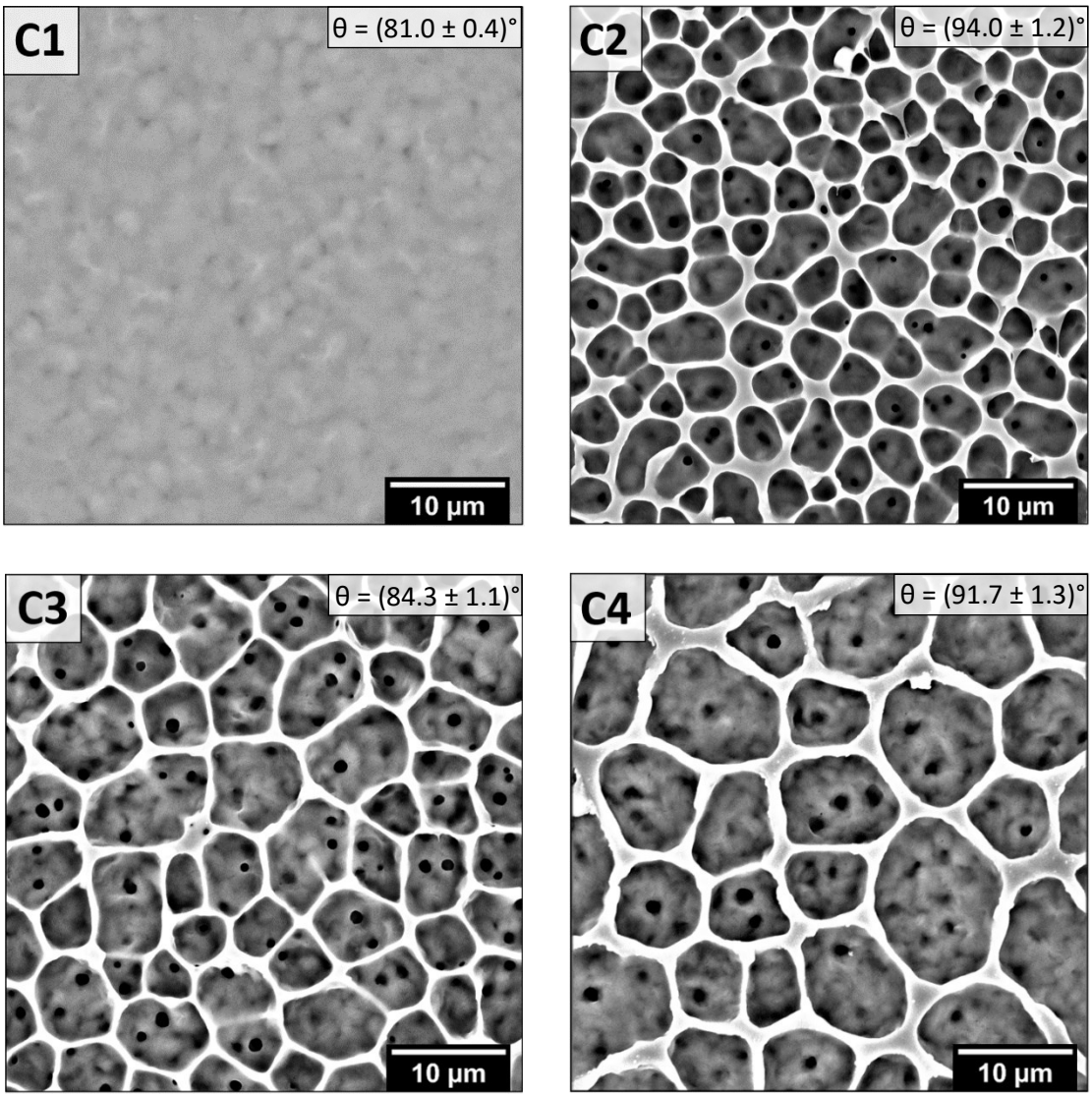

Fig. 19: SEM results of type C PCL surfaces prepared under different RHs: 15 % (C1), 35 % (C2), 50 % (C3) and 70 % (C4). Samples were prepared by dosing ***3 x 0.3 ml of THF + H_2O.***

5.1.3.1 Surface homogeneity

By "surface homogeneity" is meant evenness of the surface structure, i. e. pore size uniformity and distribution. The homogeneity evaluation was based on the visual assessment of randomly selected areas of the surface structure while examining the sample on SEM.

In the case of PCL surface type A, which is mostly composed of the aforementioned conical, sharp-peaked formations, the presence of randomly distributed non-porous areas (usually tens of micrometres in size) is evident (Fig. 20 a). This applies to PCL surface type A samples prepared under all four RHs. These non-porous areas are also present in PCL surface type B and C samples prepared under all four RHs. Additionally to these surface irregularities and also transitional structures in PCL surface type B samples prepared under RH = 15 % and RH = 35 % (Fig. 18 – B1), low RHs during PCL surface type C preparation lead to partial (under RH = 15%) or complete (under RH = 35%) destruction of porosity across the sample surface. Due to the fast evaporation rate of good solvent, a flattening of the surface occurs, resulting in a glossier appearance. High reflectivity of the flattened area is observable when the sample is positioned at the correct angle to the light. Fig. 20 shows a PCL type C sample prepared under RH = 35 % with partially destroyed porous structure:

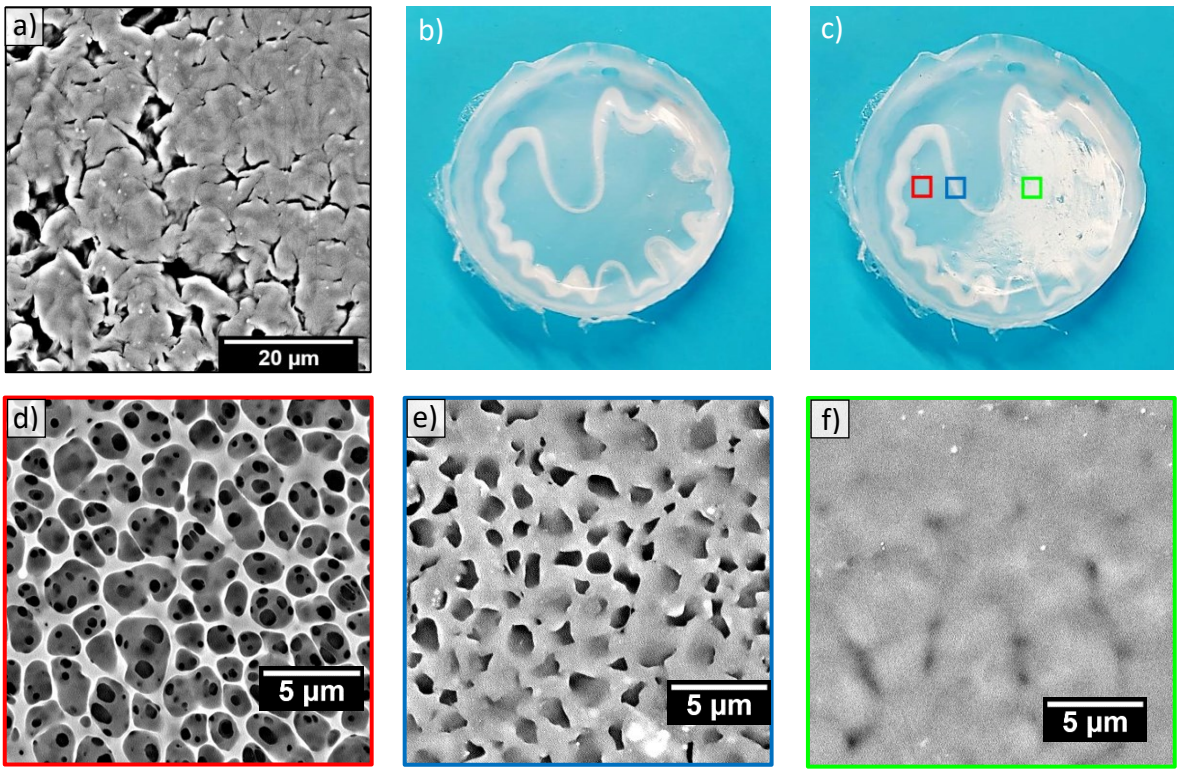

Fig. 20: SEM image of PCL surface type A prepared under RH = 50 % and photos and SEM images of PCL surface type C prepared under RH = 35 %: (a) non-porous area in PCL type A surface, (b, c) photographs of PCL surface type C and its SEM images (d, e, f).

Regarding Fig. 20, it must be noted that photographs (b) and (c) are of the same sample, except that the location of the sample in (c) is such that the flattened area reflects light from the source. SEM images (d, e, f) were taken from areas marked by squares with the corresponding colour in (c): SEM image (d) corresponding to the red square shows the porous surface structure, SEM image (e) corresponding to the blue square shows the transitional area (area with decreased porosity) and SEM image (f) corresponding to green square shows area with destroyed porosity.

If we do not consider areas with decreased porosity and band-like areas, PCL surfaces of type A prepared under all RHs and PCL surfaces of type B and C prepared at RH = 50 % and RH = 70 % exhibit approximately uniform porous structure across their entire surface. Nonetheless, this does not apply for PCL surfaces of type B and C prepared under RH = 15 % and RH = 35 % .

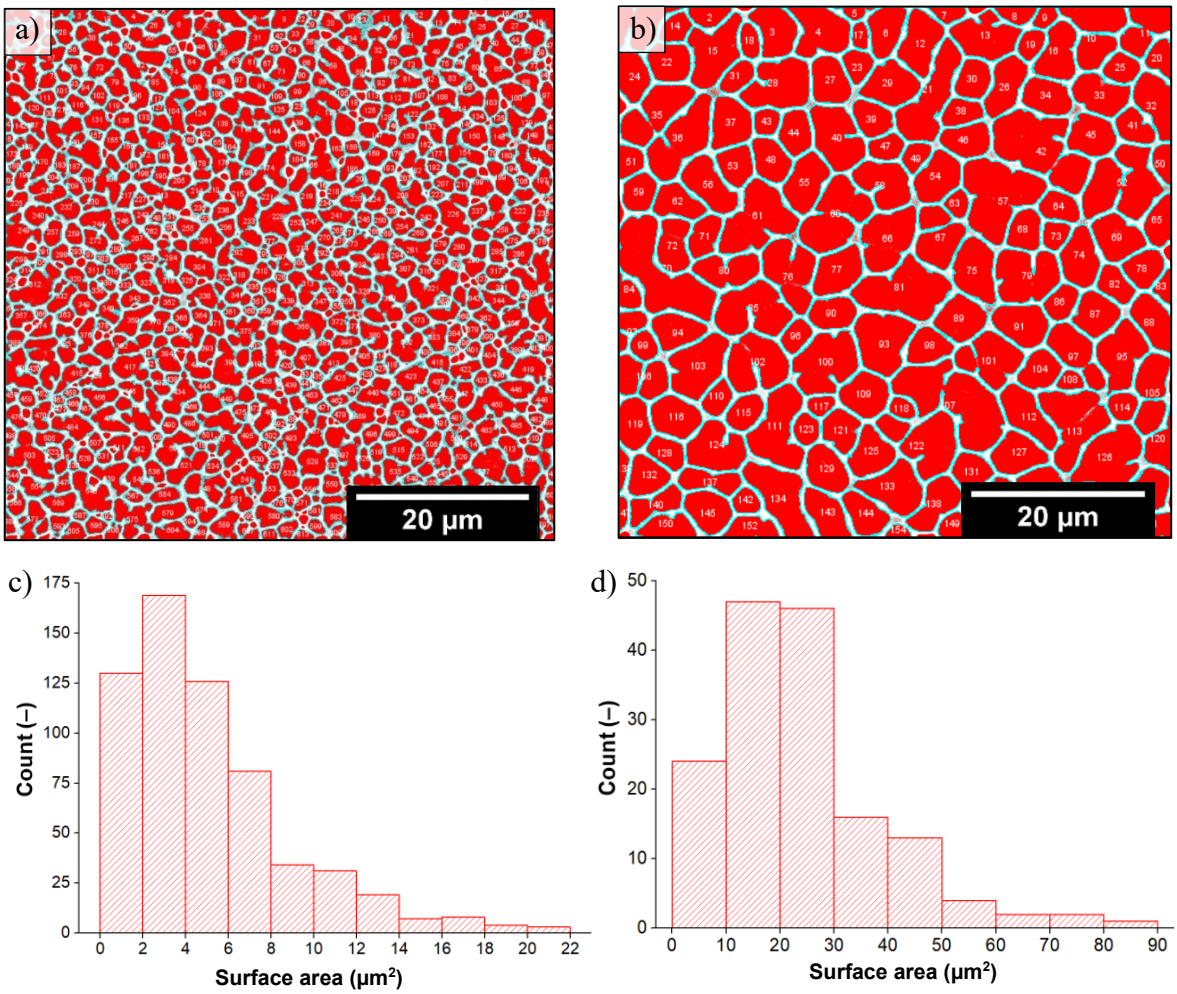

Fig. 21: Image analysis of pores size distribution of different areas of PCL surface type C sample prepared under RH = 35 %: processed SEM image (a, b), histogram of pore size distribution (c, d).

In these cases, pore size may vary significantly as the phase separation occurred unevenly due to the dissimilar evaporation rates of good solvent at different locations of the sample. Fig. 21 shows an example of extreme differences in pore size in different regions within a single PCL surface type C sample prepared under RH = 35 %. Processed SEM images (a) and (b) both cover the same surface area of 65 x 65 µm. However, total pore count in (a) is equal to 614, whereas only 155 pores cover area in (b). The histograms (c, d) display the distribution of pore sizes in areas (a, b). The x-axis represents pore size intervals ranging from 0-2 µm to 20-22 in (c) and intervals ranging from 0-10 µm 80-90 µm in (d). The y-axis represents the frequency of pores in each interval. Histogram (c) shows a prominent peak at the 2-4 µm interval, indicating 168 pores within this size range. Conversely, histogram (d) exhibits two peaks observed at intervals between 10-20 µm and 20-30 µm with 92 pores within this size ranges.

The choice of interval range was approximately determined by Sturge's rule:

$$k \approx 1 + log_2 n \tag{12}$$

where *k* is the number of intervals and *n* is the total number of data points in dataset (number of pores) [40].

The decision to represent pore size in terms of area instead of diameter was made due to the indefinite shape of the pores, which can vary in irregularity and geometry in spite of being approximately circular in shape.

5.2 Contact angle measurement

Data obtained from contact angle measurement for each surface type, i. e. type A, B, and C prepared under different humidity conditions, together with statistical processing, are shown in Table 4 in Appendix I: Contact angle measurement data and statistical processing. Table 3 on the following page sums up the results of the statistical processing of the contact angle values in the form of the mean value and the standard deviation of the mean. These results can also be seen in the previous section, with each contact angle value corresponding to the given SEM image.

Table 3: Results of contact angle measurements for PCL surfaces A, B, and C, prepared under different RH values.

RH (%) / Sample	15	35	50	70
A	$\theta = (89.9 \pm 0.6)°$	$\theta = (92.7 \pm 0.7)°$	$\theta = (93.4 \pm 0.7)°$	$\theta = (91.3 \pm 0.7)°$
B	$\theta = (94.7 \pm 0.6)°$	$\theta = (97 \pm 1)°$	$\theta = (98.5 \pm 0.7)°$	$\theta = (97.4 \pm 0.7)°$
C	$\theta = (81.0 \pm 0.4)°$	$\theta = (94.0 \pm 1.2)°$	$\theta = (84.3 \pm 1.1)°$	$\theta = (91.7 \pm 1.3)°$
C + GR			$\theta = (71.7 \pm 1.4)°$	

As can be seen from the results shown in Table 3, the contact angle values for PCL surface type A are close to 90 °, i. e. the limit value determining the wetting or non-wetting of the surface. The contact angle values for PCL surface type B imply that surface modification via the phase separation leads in all cases to a slight increase in the contact angle, compared to contact angle values of PCL surface type A. It must be noted that PCL surfaces of type B prepared under RH = 15 % and RH = 35 % (Fig. 18) still show structural similarities with PCL surface type A, thus exhibit different surface texturization from samples prepared under RH = 50 % and RH = 70 %. However, this does not lead to significant differences between the contact angles of samples prepared under different humidity conditions. In case of PCL surface type C prepared under RH = 15 %, noticeable decrease in contact angle values can be observed due to the destruction of all porosity. Contact angle values of other PCL surface type C samples do not follow any trend in terms of increase or decrease of the contact angle values, although the pore size increases with increasing RHs (Fig. 19). However, a significant change in contact angle value is evident in the case of PCL surface type C (prepared under RH = 50 %) with graphene: $\theta = (71.7 \pm 1.4)°$. This value is the only one close to the range of contact angle values preferred by cells (i. e. from 40° to 70°), and therefore among all prepared surfaces under different RHs should support the cell adhesion the most.

5.3 AFM

Fig. 22 shows AFM topography of PCL surface type C. Image (a) presents topography of 50 x 50 µm area, in which a smaller area within large pore was scanned to obtain detail of an individual pore (b). The surface morphology is also demonstrated in corresponding 3D views in (c) and (d). Triangular marks on the edges indicate the lines where the profile cuts (e, f) were made. Height profile (e) indicates that maximum pore depth across the sample surface does not exceed 3 µm. The smaller pore within the larger one is approximately 1 µm deep, as can be seen in height profile (f).

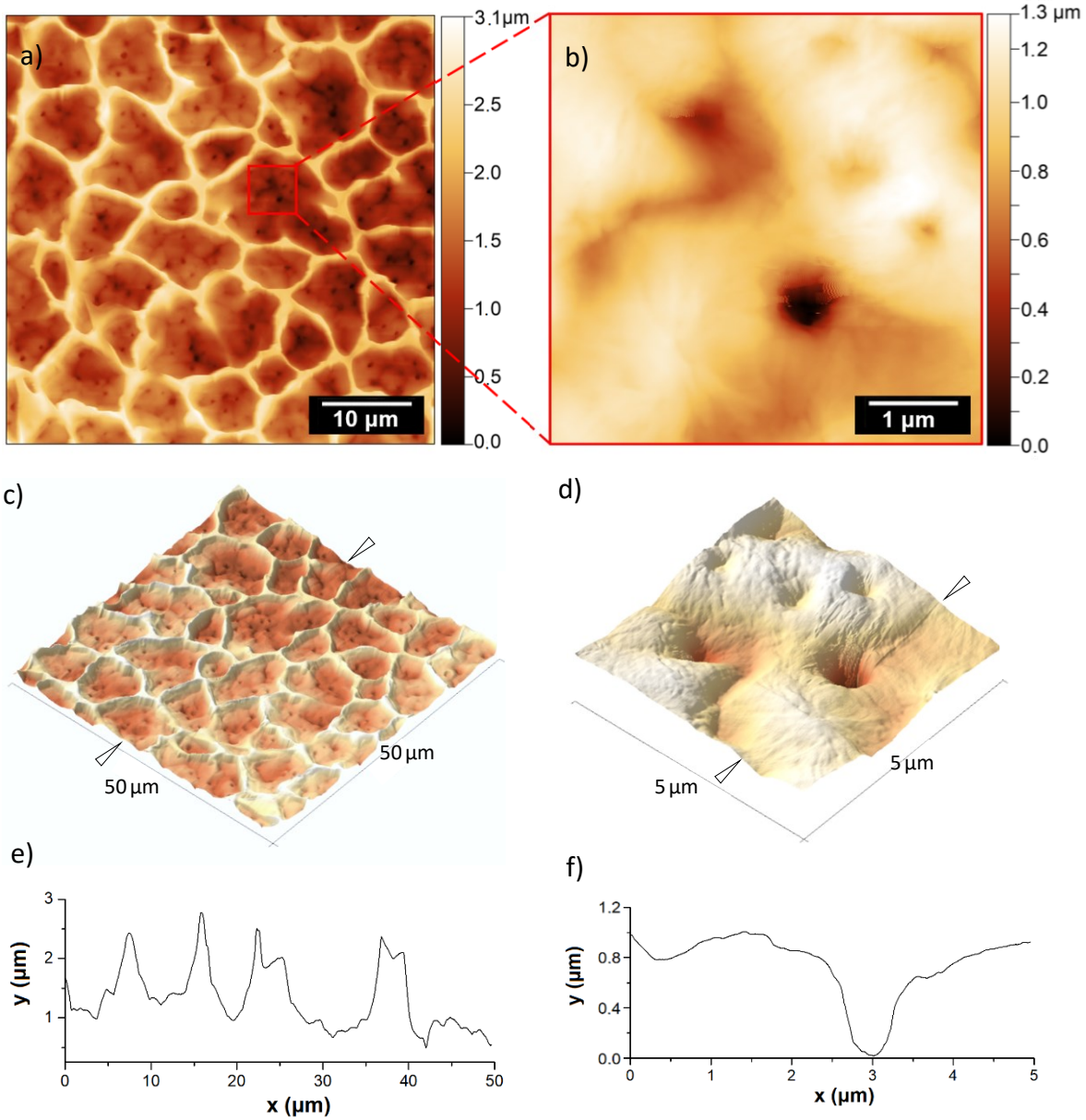

Fig. 22: AFM measurement of PCL surface type C, (a) topography of 50 x 50 µm area, (b) topography of 5 x 5 µm area with detail of an individual pore, (c, d) corresponding 3D views and (e, f) corresponding profile curves.

5.4 Raman spectroscopy

Samples of porous PCL with a graphene monolayer were investigated using confocal Raman imaging microscopy. This method combines standard confocal microscope and Raman spectrometer. Numerous scans, including both area and depth scans, were performed on samples PCL-Gr-PMMA and samples PCL-Gr. In this section, the best-obtained scanning measurement results are presented, including an example of the Raman spectrum measured at the selected point of sample PCL-Gr-PMMA in Fig. 23:

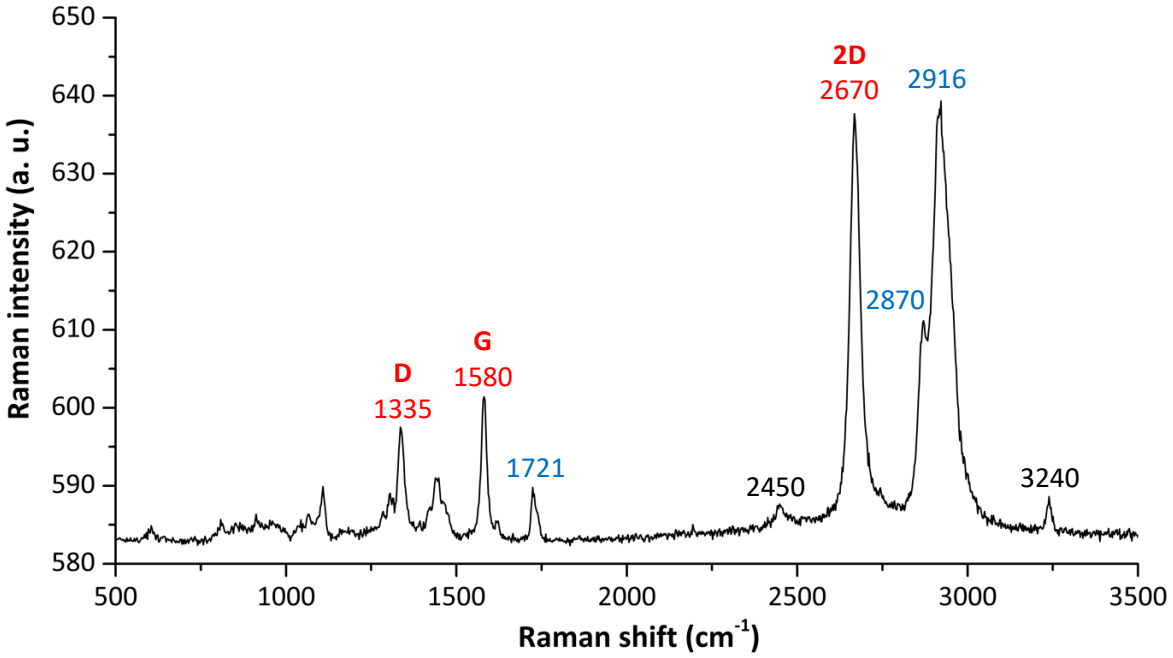

Fig. 23: Raman spectrum obtained from PCL-Gr-PMMA sample scanning: graphene bands (highlighted in red), PCL and PMMA bands (highlighted in blue) and other graphene bands (highlighted in black).

The most distinct graphene bands observed in Raman spectrum in Fig. 23 are 2D-band at 2670 cm-1 and G-band at 1580 cm^{-1}. Band intensity ratio (2D band is twice the intensity of the G band) indicates the presence of a graphene monolayer. D-band at 1335 cm^{-1} suggests that defects in graphene structure are present. Other graphene bands can be observed at 2450 cm^{-1} and 3240 cm^{-1}. However, these do not provide any significant information about the studied graphene layer. Bands at 2916 cm^{-1} and 2870 cm^{-1} correspond to the asymmetric and symmetric vibrations of the CH_2 groups in PCL and PMMA. Both polymers also contain C=O ester groups with band at 1721 cm^{-1} [41], [42], [43].

The mapping of graphene's presence within larger area regarding the sample PCL-Gr-PMMA was successfully performed by depth scanning. Fig. 24 shows thin PMMA film with graphene underneath on a porous PCL surface. For a scanning measurement, an area that was evenly attached to the PCL surface was chosen. The rainbow-like color pattern observable in (a) and (b) is an interference pattern, resulting from path difference of the light ray refraction at the air-PMMA boundary [44]. The red line in (b) indicates laser beam path during depth scanning (y-axis movement). Raman depth profiling of the sample then yields graphene's 2D band map as shown in (c). The brightest spots correspond to the highest values of Raman intensity. A straight intensity line (c) suggests that a graphene monolayer is still attached to the present PMMA, even after its transfer to the porous surface.

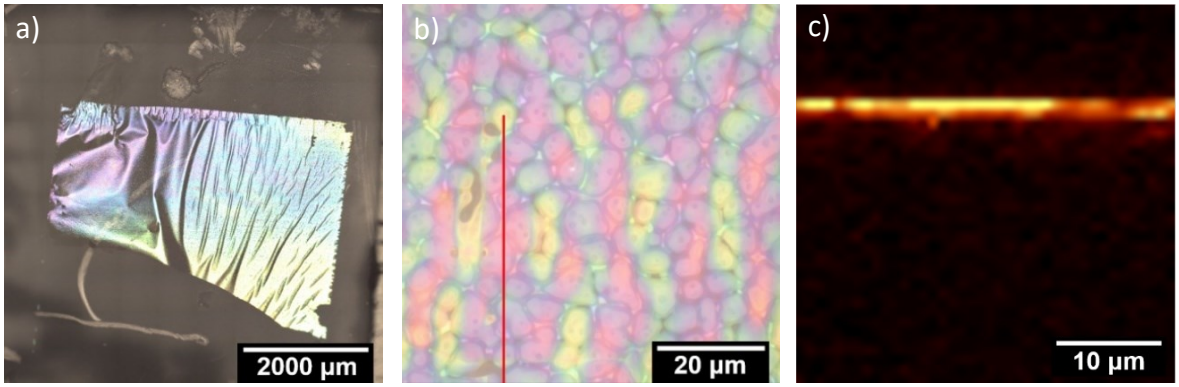

Fig. 24: Sample PCL+Gr+PMMA; a) PMMA film with graphene on a porous polymer surface, 100x magnification; b) 1000x magnification; c) 2D-band map of graphene.

In the case of sample PCL+Gr, where the PMMA-support layer was dissolved in acetone, relevant measurement results in Fig. 25 were obtained from large area scanning. Laser beam investigated are showed in (a) by scanning lines in *x* and *y*-axis while *z*-coordinate remained constant. As is apparent from the 2D-band map of graphene in (b), the graphene monolayer mostly follows the surface morphology (in contrast to the sample PCL+Gr+PMMA), as the

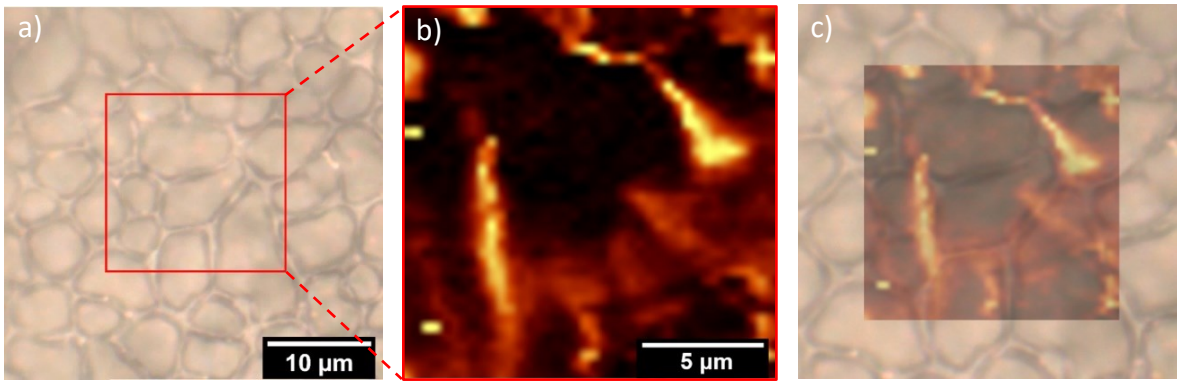

Fig. 25: Sample PCL+Gr; a) PCL surface with graphene monolayer, 1000x magnification; b) 2D-band map of graphene; c) an overlay of 2D-band map and optical microscopy image.

maximal intensity spots mostly correlate with the position of the pore edges. This can be further examined and confirmed by overlaying a partially transparent band-map image and an optical microscope image of the sample (c).

5.5 MTT assay and cell proliferation

The high adhesion of the PCL sample to the surface of the cultivation medium likely resulted in the detachment of both the cultured cells and the transferred graphene layer upon its removal from cell culture surface. As a result, the MTT assay was not conducted, as it would provide inconclusive results.

On the other hand, the comparison of cell proliferation results on PCL surface type C sample without graphene (Fig. 26) and PCL surface type C sample with graphene (Fig. 27) indicates that the presence of graphene on the porous surface significantly supports cell proliferation.

Not only is there a notable difference in the cell nucleus number observed (Hoechst) between the surface lacking graphene (Fig. 26 c) and with graphene (Fig. 27 c, d), but samples also exhibit dissimilarities in the cytoskeletal organization, with absence of cytoskeletal development (Actin Green^{TM}) evident in Fig. 26 (a, b) and mature cytoskeletal organization observed in Fig. 27 (a, b).

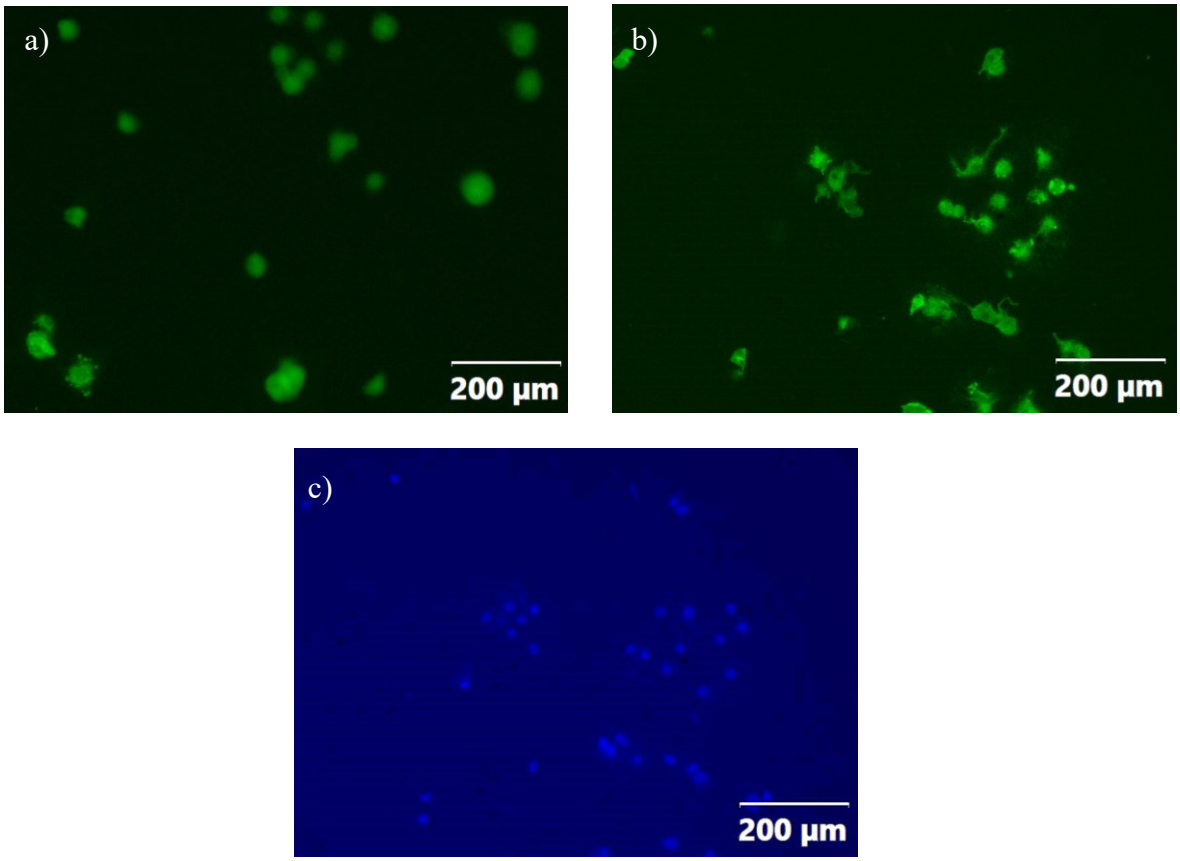

Fig. 26: Results of cell proliferation on PCL surface type C (prepared under RH = 50 %): cytoskeleton of NIH/3T3 marked in green (ActinGreen^{TM}) on sample 1 (a) and sample 2 (b), cell nuclei of NIH/3T3 marked in blue (Hoechst) on sample 1 (c).

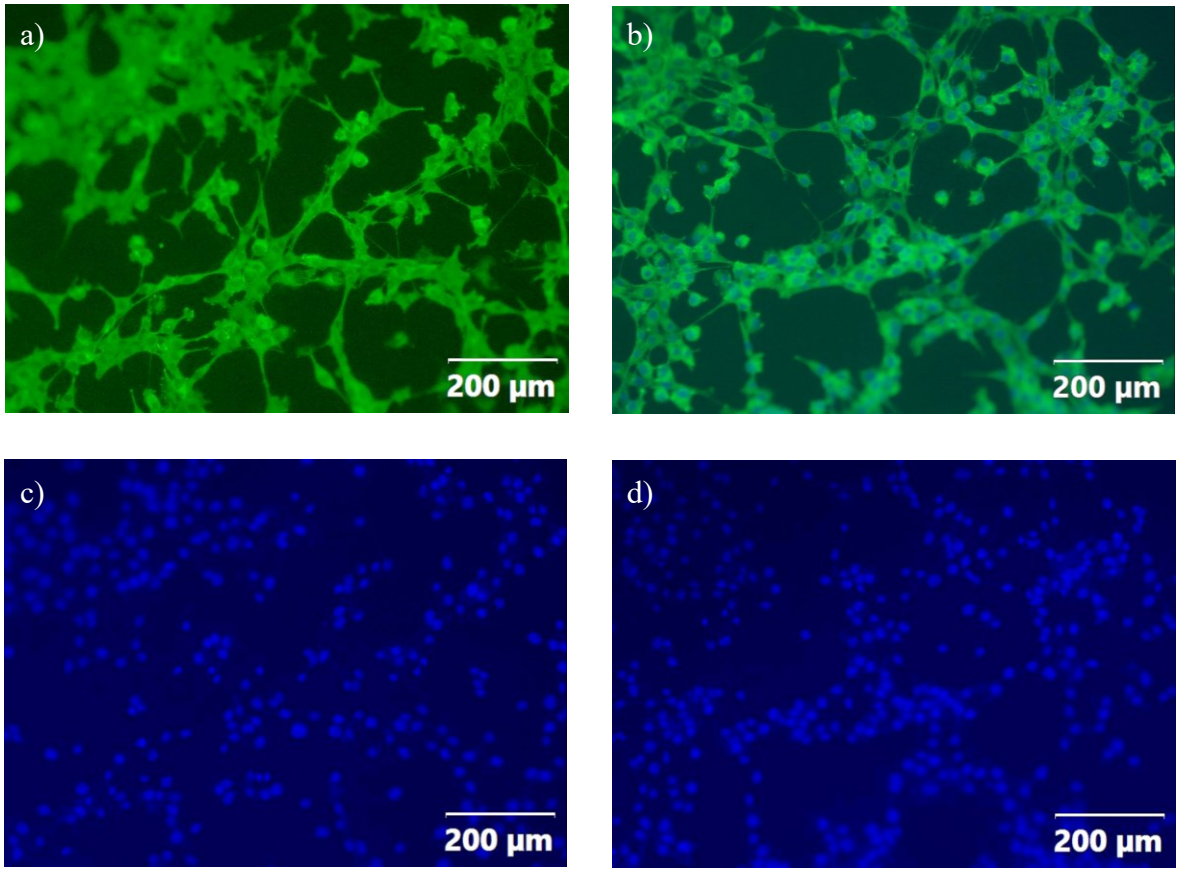

Fig. 27: Results of cell proliferation on PCL surface type C (prepared under RH = 50 %) with graphene: cytoskeleton of NIH/3T3 marked in green (ActinGreen™) on sample 1 (a) and sample 2 (b), cell nuclei of NIH/3T3 marked in blue (Hoechst) on sample 1 (c) and sample 2 (d).

6 DISCUSSION

6.1 The humidity effect on a pore size

The SEM results of PCL surface types B and C (Fig. 18 and 19) indicate a strong dependence of the resulting surface structure on humidity conditions. It is apparent that higher RHs decrease the evaporation rate of dosed solvent mixture, providing the sufficient amount of time for droplets of poor solvent to separate from solvent mixture. The obvious conclusion that the presence of air moisture slows down the evaporation rate of (in this case) organic solvents is supported by literature. This was published by Hoffman [45], mentioning that organic solvents that are immiscible with water are minimally affected by humidity conditions, whereas solvents miscible with water are significantly affected by water vapour in the surrounding air. In this case, the condition of miscibility with water is met with THF [46], as well as 2-EE [47]. In this case, both A and B meet the water miscibility condition. An example of contemporary research examining the influence of relative humidity on the evaporation rate of methanol droplet suggest that higher ambient humidity can significantly prolong the droplet lifetime. It is also observed that the influence of humidity is temperature-dependent (This dependence is particularly noticeable for lower substrate temperatures, which aligns with the temperature range established in the experimental part of this thesis) [48].

Also, the SEM observations (Fig. 18 and 19) suggest that increase in RH causes a noticeable pore size difference in case of PCL surface type C (poor solvent is water) but does not cause a significant pore enlargement in the case of PCL surface type B (poor solvent is 2-EE). This may suggest that during the dosing of solvent mixture for PCL surface type C preparation, the presence of the air humidity does not only support the surface formation by slowing down the THF evaporation rate, but also serves as a "material reservoir", enabling the growth of water droplets separated via phase separation process during dosing by potentially transferring water molecules present in vapour phase to the segregated water droplets. This assumption is supported by the work of Wrzecionko [10], where polystyrene (PS) surface structures similar to the PCL surface type C were prepared by dosing good solvent (THF) without poor solvent onto a PS surface in humid atmosphere.

The effect of air flow was not further investigated in this work, as the specific air flow value had to be set in order to maintain a constant RH during the solvent mixture deposition. This was necessary due to leaks in the constructed atmosphere chamber.

6.2 Raman spectroscopy, contact angle and biocompatibility assessment

In Fig. 24 c, the graphene's 2D-band mapping result suggests that the thickness of the graphene is greater than what would be expected for a monolayer. This is primarily due to optical aberrations of the Raman microscope and the size of the laser beam spot.

The number of measured contact angle values for each sample is low due to the limited sample dimensions. Measured values can also be influenced by the degree of surface homogeneity and the presence of macro-corrugation on the sample. However, there is a noticeable difference in the contact angle attributed to the presence of graphene, which is likely responsible for the enhanced cell proliferation observed on the PCL surface type C sample with graphene. Furthermore, additional research should explore alternative methods to enhance cell adhesion on the surface, such as surface plasma treatment. It should also be investigated whether a decrease in contact angle through plasma treatment could yield similar cell proliferation results to those observed on the sample with graphene. Future studies should also explore the cell proliferation potential of other samples (PCL surface type A and B) that were not examined in this study.

CONCLUSION

The aim of this thesis was the preparation of suitable porous polycaprolactone surfaces and the investigation of whether graphene's presence could support the biocompatibility of such surfaces. The theoretical part investigated the preparation procedures of porous surfaces using the breath figure method and phase separation induced by time-sequenced dosing of mixed solvent. It also included a brief overview of the thermodynamical background regarding polymer solutions, as well as a theory of graphene and experimental methods used in this work.

The experimental results of this work showed that surface modification of PCL surfaces via phase separation showed high humidity dependence. While low RHs resulted in uneven surface texturization and, in certain cases, to complete destruction of porosity, higher RHs demonstrated desirable outcomes. The optimal surface texturization was observed at RH = 50 %.

The wettability of prepared porous PCL surfaces was characterized by contact angle measurement. The majority of the prepared structures displayed a slightly hydrophobic nature, with their contact being slightly above 90° and occasionally exceeding 80°. The presence of graphene resulted in a decrease of contact angle to approximately 70°, which is considered the upper limit preferred by cells.

A CVD-grown graphene monolayer was transferred to the samples of chosen PCL surface type using the wet transfer method. Graphene's presence and positioning on the porous surface was investigated by Raman spectroscopy. The Raman intensity ratio of graphene's 2D-band and G-band suggested that only a monoatomic layer is present, with D-band, however, indicating defects in the lattice structure. The Raman band mapping confirmed attachment to a supporting PMMA layer. After the PMMA layer removal, the Raman band mapping showed that graphene is placed on pore edges.

The MTT assessment was not possible due to an incorrectly chosen procedure. However, cell proliferation using mouse fibroblasts yielded notable results. The surface with graphene demonstrated a significant improvement in the number of cell nuclei and the degree of cytoskeletal development compared to the surface without graphene. Therefore, based on the small number of performed proliferation tests, these results suggest that graphene enhances cell adhesion and proliferation, thus resulting in the biocompatibility enhancement of a porous polycaprolactone surface.

BIBLIOGRAPHY

[1] WU, Dingcai et al. Design and Preparation of Porous Polymers. Chemical Reviews 2012 112 (7), 3959-4015. DOI:10.1021/cr200440z

[2] TORUN, Neslihan et al. Physically unclonable surfaces via dewetting of polymer thin films. American Chemical Society (ACS), 2021. 11247 s. ISBN 1944-8244. DOI: 10.1021/acsami.0c16846

[3] CHEN, G. a N. KAWAZOE. Characterisation and design of tissue scaffolds. Elsevier Ltd. , 20165 - Preparation of polymer-based porous scaffolds for tissue engineering. 105-125 s. ISBN 9781782420873. DOI: 10.1016/B978-1-78242-087-3.00005-5

[4] ROUQUEROL, J. et al. Recommendations for the chraracterization of porous solids (Technical report).Pure & Appl. Chern., Vol. 66, No. 8, pp. 1739-1758, 1994. DOI: 10.1351/pac199466081739

[5] WRZECIONKO, Erik et al. Variations of polymer porous surface structures via the time-sequenced dosing of mixed solvents. ACS Appl Mater. Interfaces, 2017. 6472 s. ISBN 1944-8244. DOI: 10.1021/acsami.6b15774

[6] DOU, Yingying et al. Breath Figure Method for Construction of Honeycomb Films. Membranes. 2015, vol. 5, no. 3, s. 399-424. ISSN 2077-0375. DOI: 10.3390/membranes5030399

[7] MUÑOZ-BONILLA, Alexandra, Marta FERNÁNDEZ-GARCÍA a Juan RODRÍGUEZ-HERNÁNDEZ. Towards hierarchically ordered functional porous polymeric surfaces prepared by the breath figures approach. Progress in Polymer Science [online]. 2014, vol. 39, no. 3, s. 510-554. ISSN 0079-6700. Dostupné z: https://www.sciencedirect.com/science/article/pii/S0079670013001032

[8] FALAK, Shahkar, Bokyoung SHIN a Dosung HUH. Modified Breath Figure Methods for the Pore-Selective Functionalization of Honeycomb-Patterned Porous Polymer Films. Nanomaterials (Basel, Switzerland) [online]. 2022, vol. 12, no. 7, s. 1055. ISSN 2079-4991. Dostupné z: https://www.mdpi.com/2079-4991/12/7/1055

[9] SRINIVASARAO, Mohan et al. Three-Dimensionally Ordered Array of Air Bubbles in a Polymer Film. Science. 2001, vol. 292, no. 5514, s. 79-83. ISSN 0036-8075. DOI: 10.1126/science.1057887

[10] WRZECIONKO, Erik. Příprava a charakterizace hierarchicky organizovaných funkčních polymerních vrstev a porózních systémů. Zlín, 2021. Dizertační práce. Univerzita Tomáše Bati ve Zlíně, Fakulta Technologická. Vedoucí práce Antonín Minařík.

[11] MILLER-CHOU, Beth A. a Jack L. KOENIG. A review of polymer dissolution. Elsevier BV, 2003. 1223 s. ISBN 0079-6700. DOI: 10.1016/S0079-6700(03)00045-5

[12] OVEJERO, G. et al. Solubility and Flory Huggins parameters of SBES, poly(styrene-b-butene/ethylene-b-styrene) triblock copolymer, determined by intrinsic viscosity. European Polymer Journal. 2007, vol. 43, no. 4, s. 1444-1449. ISSN 0014-3057. DOI: 10.1016/j.eurpolymj.2007.01.007

[13] BRANDRUP, J., E. H. IMMERGUT a E. A. GRULKE. Polymer Handbook. Vol. 2, 4th Ed. New York: Wiley & Sons, 2003. ISBN 978-0-471-47936-9.

[14] FAN, Cun Feng et al. Application of molecular simulation to derive phase diagrams of binary mixtures. Macromolecules. 1992, vol. 25, no. 14, s. 3667-3676. ISSN 0024-9297. DOI: 10.1021/ma00040a010

[15] TERAOKA, Iwao. Polymer solutions: an introduction to physical properties. New York: Wiley & Sons, 2002. ISBN 978-0-471-38929-3.

[16] STOKLASA, Karel. Makromolekulární chemie I. Učební texty Univerzity T. Bati ve Zlíně, 2005, 106 s.

[17] BANDYOPADHYAY, A., Bose, S. Characterization of biomaterials. Elsevier Inc., Pullman WA, 2013. ISBN: 9781493301379

[18] GHASEMI, Mahshid et al. The MTT Assay: Utility, Limitations, Pitfalls, and Interpretation in Bulk and Single-Cell Analysis. International Journal of Molecular Sciences. 2021, vol. 22, no. 23, s. 12827. ISSN 1422-0067. DOI: 10.3390/ijms222312827

[19] MALÍK, Antonín. Biologické vlastnosti hydrogelových filmů pro hojení ran. Diplomová práce. Univerzita Tomáše Bati ve Zlíně, Fakulta Technologická. Vedoucí práce: Zdenka Capáková.

[20] DESHMUKH, K. et al. Biopolymer composites in Electronics. Elsevier Inc., 20173 - Biopolymer Composites With High Dielectric Performance: Interface Engineering. . 27-128 s. ISBN 0128092610. DOI: 10.1016/B978-0-12-809261-3.00003-6

[21] ZHANG, F. et al., Recent advances on graphene: Synthesis, properties and applications. Applied Science and Manufacturing, Applied science and manufacturing, vol. 6 160, 2022, 107051. ISSN: 1359-835 X. DOI: 10.1016/j.compositesa.2022.107051

[22] GEIM, A. K., NOVOSELOV, K. S. The Rise of Graphene. Nature Materials. 2007, vol. 6, no. 6, s. 183-191. ISSN 1476-1122. DOI: 10.1038/nmat1849

[23] NOVOSELOV, K. S. et al. A roadmap for graphene. Nature. 2012, vol. 490, no. 7419, s. 192-200. ISSN 0028-0836. DOI: 10.1038/nature11458

[24] Abid et al. Reduced graphene oxide (rGO) based wideband optical sensor and the role of Temperature, Defect States and Quantum Efficiency. Scientific Reports. 2018, vol. 8, no. 1, s. 3537-13. ISSN 2045-2322. DOI: 10.1038/s41598-018-21686-2

[25] ALLEN, Matthew J., Vincent C. TUNG a Richard B. KANER. Honeycomb Carbon: A Review of Graphene. Chemical Reviews. 2010, vol. 110, no. 1, s. 132-145. ISSN 0009-2665. DOI: 10.1021/cr900070d

[26] PROCHÁZKA, Pavel. Příprava grafenu metodou CVD. Diplomová práce. Vysoké učerní technické v Brně, Fakulta strojního inženýrství. Vedoucí práce: Jindřich mach.

[27] ZHANG, Yi, Luyao ZHANG a Chongwu ZHOU. Review of Chemical Vapor Deposition of Graphene and Related Applications. Accounts of Chemical Research. 2013, vol. 46, no. 10, s. 2329-2339. ISSN 0001-4842. DOI: 10.1021/ar300203n

[28] GRAY, N. Knowing the limit. Nat Cell Biol 11 (Suppl 1), S8 (2009). DOI: 10.1038/ncb1940

[29] VERNON-PARRY, K. D.,Scanning electron microscopy: An introduction K D vernon-parry, centre for electronic materials, UMIST I. DOI: 10.1016/S0961-1290(00)80006-X

[30] Wikimedia Commons contributors, Interaction. 2020. [online]. Available from: https://commons.wikimedia.org/wiki/File:Interaction.png

[31] ROSE, Harald. Aberration correction in electron microscopy. International Journal of Materials Research. 2022, vol. 97, no. 7, s. 885-889. ISSN 1862-5282. DOI: 10.1515/ijmr-2006-0143

[32] MACHALA, Libor et. al. Mikroskopie skenující sondou. Univerzita Palackého v Olomouci. Olomouc, 2003.

[33] YASAKAU, Kiryl. Application of AFM-Based Techniques in Studies of Corrosion and Corrosion Inhibition of Metallic Alloys. Corrosion and Materials Degradation. 2020, vol. 1, no. 3, s. 345-372. ISSN 2624-5558. DOI: 10.3390/cmd1030017

[34] LE PEVELEN, D. D. Encyclopedia of spectroscopy and spektrometry. Third Edition. Elsevier Ltd., 2017 NIR FT-Raman. 98-109 s. ISBN 0128032251. DOI: 10.1016/B978-0-12-409547-2.12150-X.

[35] ANDREWS, David L. Encyclopedia of spectroscopy and spektrometry. Third Edition. Elsevier Ltd. , 2017. Rayleigh Scattering and Raman Effect, Theory. 924-930 s. ISBN 0128032251. DOI: 10.1016/B978-0-12-409547-2.11337-X.

[36] GERALDES, Carlos F. G. C. Introduction to infrared and raman-based biomedical molecular imaging and comparison with other modalities. MDPI AG, 2020. Available from: DOI: 10.3390/molecules25235547

[37] ORLANDO, Andrea et al. A Comprehensive Review on Raman Spectroscopy Applications. Chemosensors. 2021, vol. 9, no. 9, s. 262. ISSN 2227-9040. DOI: 10.3390/chemosensors9090262

[38] BARTOVSKÁ, L., ŠIŠKOVÁ, M. Fyzikální chemie povrchů a koloidních soustav. VŠCHT Praha, 2010.

[39] ARIMA, Y. IWATE H. Effect of wettability and surface functional groups on protein adsorption and cell adhesion using well-defined mixed self-assembled monolayers. Biomaterials. 2007, vol. 28, no. 20, s. 3074-3082. ISSN 0142-9612. DOI: 10.1016/j.biomaterials.2007.03.013

[40] AGGOGERI, Francesco et al. Statistical Modeling of Industrial Process Parameters. Procedia CIRP. 2015, vol. 33, s. 203-208. ISSN 2212-8271. DOI: 10.1016/j.procir.2015.06.037

[41] HELLER, Eric J. et al. Theory of Graphene Raman Scattering. ACS Nano. 2016, vol. 10, no. 2, s. 2803-2818. ISSN 1936-0851. DOI: 10.1021/acsnano.5b07676.

[42] UNALAN, Irem et al. Physical and Antibacterial Properties of Peppermint Essential Oil Loaded Poly (ε-caprolactone) (PCL) Electrospun Fiber Mats for Wound Healing.

Frontiers in Bioengineering and Biotechnology. 2019, vol. 7, s. 346. ISSN 2296-4185. DOI: 10.3389/fbioe.2019.00346

[43] MALARD, L. M. et al. Raman spectroscopy in graphene. Physics Reports. 2009, vol. 473, no. 5, s. 51-87. ISSN 0370-1573. DOI: 10.1016/j.physrep.2009.02.003

[44] ABAS, Ahmad Fauzi et al. Dispersion Management and Pulse Characterization of Graphene-Based Soliton Mode-Locked Fiber Lasers. Applied Sciences. 2022, vol. 12, no. 7, s. 3288. ISSN 2076-3417. DOI: 10.3390/app12073288.

[45] HOFMANN, Harry E. Evaporation Rates of Organic Liquids. Industrial and Engineering Chemistry. 1932, vol. 24, no. 2, s. 135-140. ISSN 0019-7866. DOI: 10.1021/ie50266a004.

[46] PAROD, R. J. Encyclopedia of toxicology. Third Edition. Elsevier Inc., 2014. Tetrahydrofuran. 505-508 s. ISBN 0123864542. DOI: 10.1016/B978-0-12-386454-3.00437-1 505

[47] STANDARD, B. Ethoxyethanol. Encyclopedia of Toxicology. Second edition. Elsevier Inc., 2005. Ethoxyethanol. 274-276 s. ISBN 9780123694003. DOI: 10.1016/B0-12-369400-0/00389-6.

[48] ANDALIB, S. et al. Combined effect of relative humidity and substrate temperature on evaporation of methanol droplet. JCT Research. 2019, vol. 16, no. 6, s. 1691-1698. ISSN 1547-0091. DOI: 10.1007/s11998-019-00271-w

[49] BUDÍKOVÁ, M et al. Průvodce základními statistickými metodami. Praha: Grada, 2010. Expert (Grada). ISBN 978-80-247-3243-5.

LIST OF ABBREVIATIONS

IUPAC	International Union of Pure and Applied Chemistry
PUF	Physically unclonable function
BF	Breath figuers
THF	Tetrahydrofuran
2-EE	2-Ethoxyethanol
PS	Polystyrene
RH	Relative humidity
RHs	Relative humidites
ΔG_m	Gibbs free change energy of mixing
ΔH_m	Enthalpy change of mixing
T	Thermodynamic temperature
ΔS_m	Entropy change of mixing
ϕ	Volume fraction
R	Molar gas constant
x	Chain length
ω	Interaction energy parameter
χ	Flory–Huggins parameter
Z	Lattice coordinate
k_B	Boltzman constant
δ	Hildebrand solubility parameter
ΔE	Cohesive energy density
V	Volume
MTT	Methyl-thiazolyl-tetrazolium
DMSO	Dimethyl sulfoxide
PCL	Polycaprolactone

CVD	Chemical vapour deposition
BSE	Backscattered electrons
SE	Secondary electron
AFM	Atomic force microscopy
L-J, U	Lennard-Jones potential
ε	Specific L–J parameter
r	Interatomic distance
E	Energy of scattered photon
h	Planck constant
ν	Frequency of photon
W	Work
γ	Surface energy, surface tension
A	Area
F	Force
L	Length
s	Solid, second
l	Liquid
g	Gas
RPM	Revolutions per minute
TSSC	Time sequenced spin coater
SEM	Scanning electron microscopy
PMMA	Polymethylmethacrylate
Gr, GR	Graphene
μ	Mean value
σ	Standard deviation
G	G-value

LIST OF FIGURES

LIST OF TABLES

APPENDICES

Appendix I: Contact angle measurement data and statistical processing

The following table shows obtained results of contact angle of water on various porous PCL surfaces. Due to the relatively small area of PCL films with porous surface, which is determined by the diameter of Petri dish and volume of dosed solvent mixture, the measurement could provide maximum of 10 relevant contact angle values per sample. Statistical processing of the results, shown in the table 4, detected outliers using Grubbs' test for outliers, resulting in their exclusion from the statistical set. For the set of measured contact angle values, the mean value μ of the contact angle for each surface type was determined along with the sample standard deviation σ and standard deviation of the mean σ_μ.

The mean value and standard deviation of the mean were determined after the outliers were excluded from the data set via the Grubb's test. Outliers (shown in the following table) are highlighted in red. In the case of 10 contact angle values in each data set, the critical value with significance level $\alpha = 0.05$ is equal to 2.29 [budíková 2010]. The G-value is then calculated as:

$$G = \frac{|x - \mu|}{\sigma} \tag{13}$$

where x is the maximum or minimum value from data set. If the G-value is greater than the critical value, the value being tested is considered an outlier [49].

Table 4: Obtained contact angle measurement values

sample	A1	A2	A3	A4	B1	B2	B3
1	87.46	89.61	90.30	89.02	91.88	91.71	94.86
2	88.41	89.97	90.92	89.21	92.29	94.26	96.58
3	88.56	90.61	91.78	89.60	93.27	94.29	97.14
4	89.14	92.73	92.85	89.63	93.68	96.02	97.52
5	90.18	92.82	93.20	89.98	95.44	96.42	98.54
6	91.03	93.21	93.49	91.32	95.59	97.08	99.23
7	91.13	93.38	93.57	92.26	95.76	99.04	99.79
8	91.45	94.44	93.75	93.06	95.91	99.26	99.82
9	91.57	94.79	96.25	93.54	96.01	100.38	100.63
10	96.38	95.07	97.49	95.17	96.42	101.31	100.84
μ	89.88	92.66	93.36	91.28	94.63	96.98	98.49
σ	1.52	1.98	2.20	2.13	1.68	3.04	1.94
σ_μ	0.51	0.62	0.70	0.67	0.53	0.96	0.61
$\mu \pm \sigma_\mu$	89.9 ± 0.6	92.7 ± 0.7	93.4 ± 0.7	91.3 ± 0.7	94.7 ± 0.6	97 ± 1	98.5 ± 0.7

sample	B4	C1	C2	C3	C4	C + GRA
1	93.81	79.07	89.17	79.29	85.90	66.08
2	94.45	80.01	89.67	80.51	86.55	66.61
3	96.03	80.10	90.27	81.76	88.12	67.94
4	96.07	80.17	91.25	83.15	88.70	67.97
5	97.72	81.13	92.93	84.06	92.63	70.52
6	98.59	81.27	95.30	84.08	93.07	73.24
7	98.69	81.37	96.45	85.60	94.07	74.43
8	98.79	81.48	96.61	85.64	95.55	74.89
9	99.40	82.05	98.37	88.99	95.71	76.79
10	99.77	82.63	99.07	89.64	96.16	77.59
μ	97.33	80.93	93.91	84.27	91.65	71.61
σ	2.11	1.07	3.71	3.36	3.96	4.31
σ_μ	0.67	0.34	1.17	1.06	1.25	1.36
$\mu \pm \sigma_\mu$	97.4 ± 0.7	81.0 ± 0.4	94.0 ± 1.2	84.3 ± 1.1	91.7 ± 1.3	71.7 ± 1.4

The only value that was detected as an outlier and therefore excluded from the dataset is highlighted in red.

Appendix II: SEM images of PCL surfaces (type A, B, C), four different magnifications

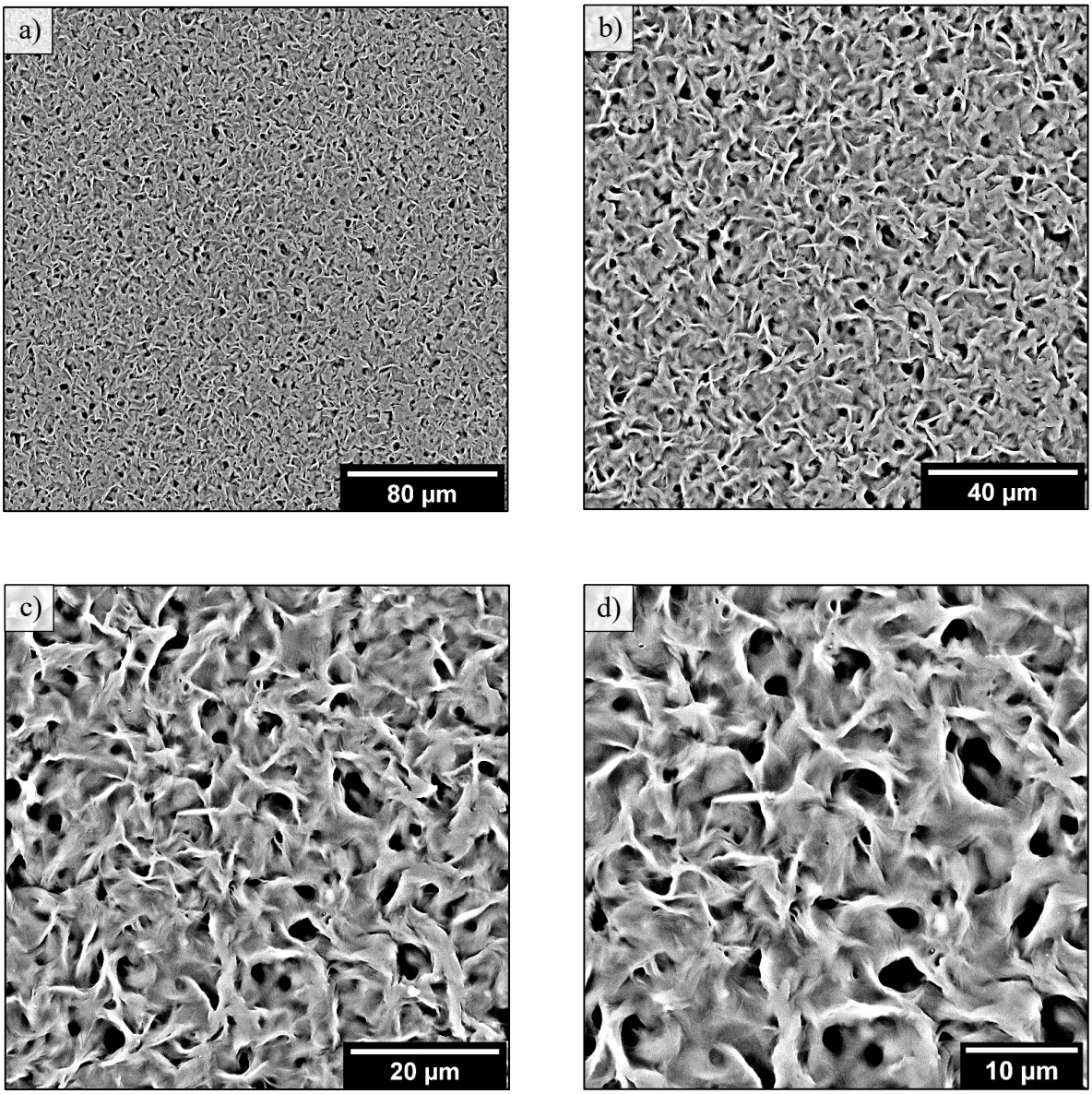

Fig. 28: SEM images of PCL surface type A prepared under RH = 50 %, (a) 1000x magnification, (b) 2000x magnification, (c) 4000x magnification, (d) 6000x magnification.

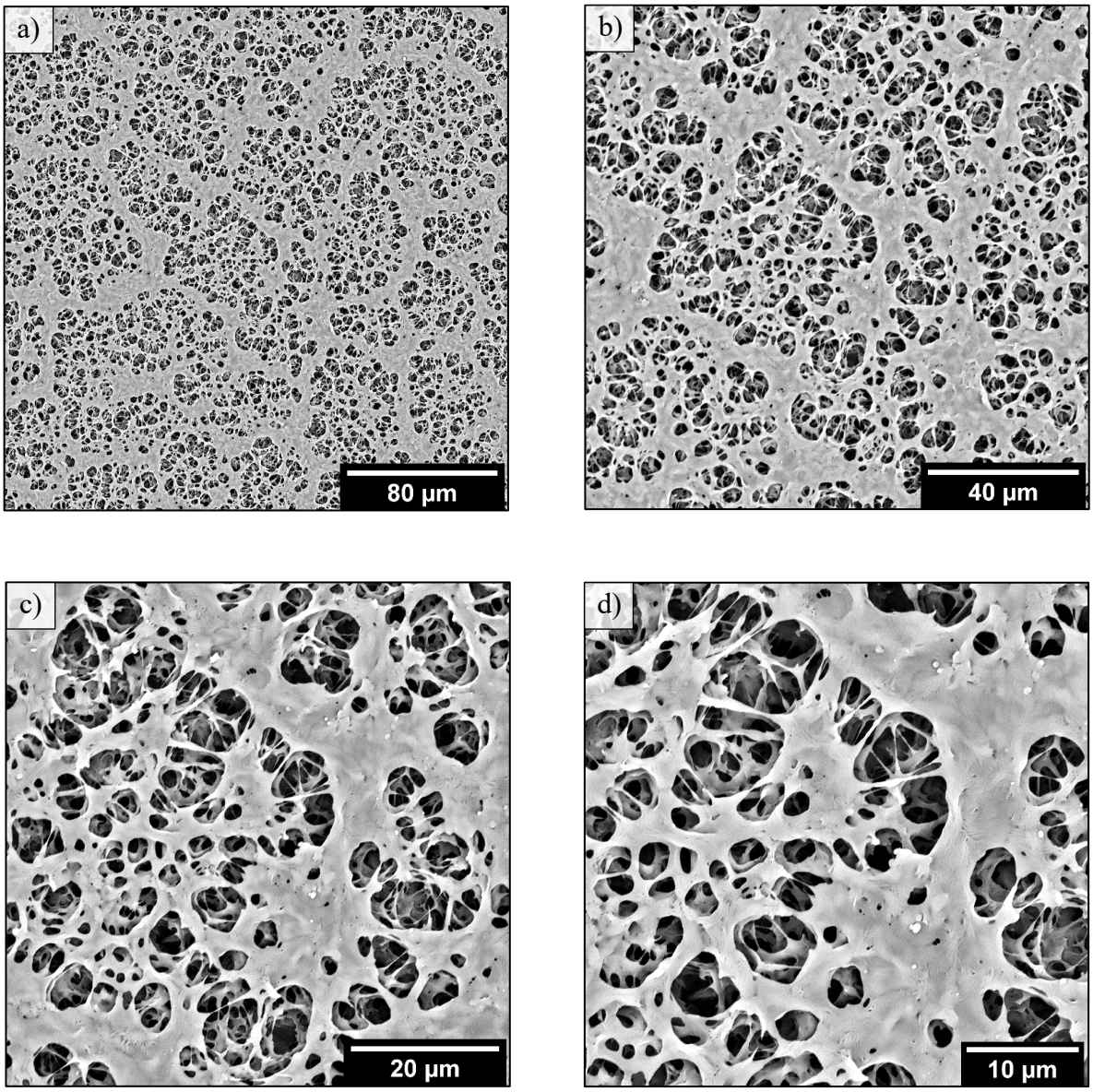

Fig. 29: SEM images of PCL surface type B prepared under RH = 50 %, (a) 1000x magnification, (b) 2000x magnification, (c) 4000x magnification, (d) 6000x magnification.

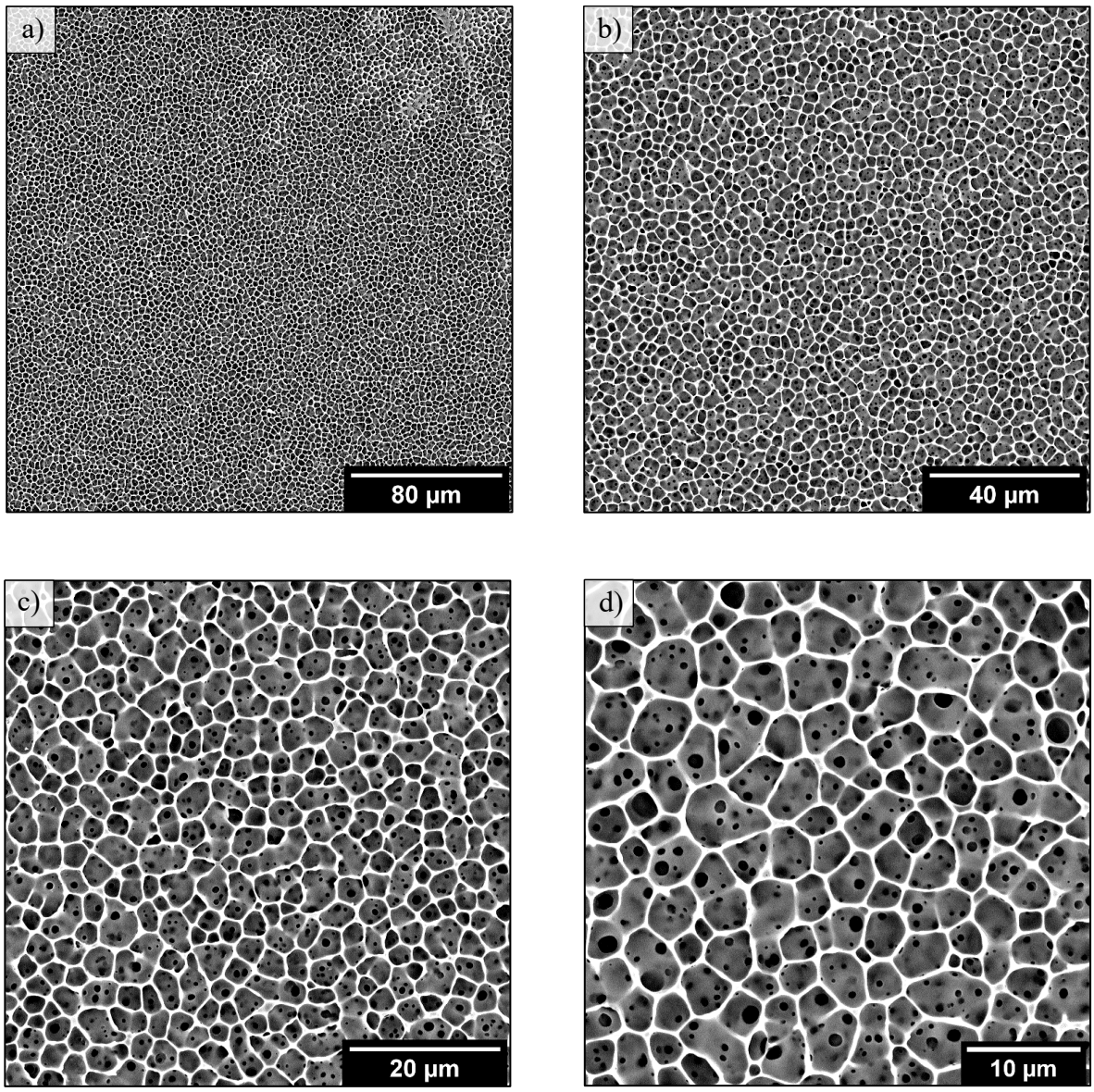

Fig. 30: SEM images of PCL surface type C prepared under RH = 50 %, (a) 1000x magnification, (b) 2000x magnification, (c) 4000x magnification, (d) 6000x magnification.